

# Probing the Solar Corona at High Temporal and Spatial Resolution with the LOw Frequency ARray (LOFAR)

A dissertation submitted to the University of Dublin  
for the degree of Doctor of Philosophy

**Pearse Murphy, B.A. (Mod.)**

*School of Physics, Trinity College Dublin*

*Supervisor:*

Prof. Peter T. Gallagher

*Co-Supervisor:*

Dr. Eoin P. Carley

**December 2021**



**Trinity College Dublin**

Coláiste na Tríonóide, Baile Átha Cliath

The University of Dublin



## Summary

The solar corona is the outermost layer of the Sun's atmosphere. Advancements in radio astronomy over the last 50 years have revealed a number of radio phenomena which occur in the corona each with different temporal and spectral characteristics. Current generation interferometers such as the LOw Frequency ARray (LOFAR) give an unprecedented insight into the fine structure of these radio bursts. Of particular interest are what are known as Type III radio bursts. These are indicative of electrons being accelerated along open magnetic field lines in the solar corona. Particularly bright radio bursts can have devastating effects on terrestrial communication including GPS positioning and satellite communication. Given that much of modern society relies on satellite communication, being better able to understand and perhaps predict radio bursts is essential. High temporal resolution data allow the study of rapid temporal variability in radio spectra which are indicative of small-scale turbulence in the solar corona. It is thought that the density inhomogeneities produced by this small-scale turbulence causes scattering of radio waves as they propagate out from the corona and thus pose a fundamental limit on the source size of observed radio bursts. Analysis of a radio burst at the plasma frequency, such as a Type III burst, with highly spatially resolved interferometric data is the most direct way of testing this hypothesis.

The nature of this PhD is twofold, firstly to observe low frequency radio emission from the Sun at spatial resolution of the order of 15 arcseconds. This will determine whether or not scattering of radio waves in the corona imposes a fundamental limit on spatial resolution and give insight into the processes that might cause this limit. The second aspect of this PhD is to observe the Sun at radio wavelengths at the highest temporal resolution ever. In order to do this, the TBB Acquisition Cluster (TACl) located in the I-LOFAR control room must be further developed to record and store TBB data without corruption. Observing the Sun at nanosecond temporal resolution has yet to be attempted and as such the potential to discover new radio phenomena and temporal variability in existing phenomena is great. It is, of course, possible that such events do not occur or are difficult to detect and as such the focus for this PhD will lie mainly on interferometric observations of the Sun.

## **Declaration**

I have read and I understand the plagiarism provisions in the General Regulations of the University Calendar for the current year, found at:  
<https://www.tcd.ie/calendar>

I have also completed the Online Tutorial on avoiding plagiarism ‘Ready, Steady, Write’, located at <http://tcd-ie.libguides.com/plagiarism/ready-steady-write>

I declare that this report is my own work, is not copied from any other person’s work (published or unpublished), and has not previously submitted for assessment either at Trinity College Dublin or elsewhere.

**Name:** Pearse Murphy

**Signature:** ..... **Date:** .....

# List of Publications

## Publications

1. **P. C. Murphy**, P. Callanan, J. McCauley, D. J. McKenna, D. Ó Fionnagáin, C. K. Louis, M. P. Redman, L. A. Cañizares, E. P. Carley, S. A. Maloney, B. Coghlan, M. Daly, J. Scully, J. Dooley, V. Gajjar, C. Giese, A. Brennan, E. F. Keane, C. A. Maguire, J. Quinn, S. Mooney, A. M. Ryan, J. Walsh, C. M. Jackman, A. Golden, T. P. Ray, J. G. Doyle, J. Rigney, M. Burton, P. T. Gallagher.  
“First Results from the REAL-time Transient Acquisition backend (REALTA) at the Irish LOFAR station”,  
*Astronomy and Astrophysics* (accepted 2021)
2. A. M. Ryan, P. T. Gallagher, E. P. Carley, M. A. Brentjens, **P. C. Murphy**, C. Vocks, D. E. Morosan, H. Reid, J. Magdalenic, F. Breitling, P. Zucca, R. Fallows, G. Mann, A. Kerdraon, R. Halfwerk.  
“LOFAR imaging of the solar corona during the 2015 March 20 solar eclipse”,  
*Astronomy and Astrophysics*, Volume 648, A43 (2021)
3. **Pearse C. Murphy**, Eoin P. Carely, Aoife Maria Ryan, Pietro Zucca, Peter T. Gallagher.  
“LOFAR Observations of Radio Burst Source Sizes and Scattering in the Solar Corona”,  
*Astronomy and Astrophysics*, Volume 645, A11 (2021)
4. Vishal Gajjar, Andrew Siemion, Steve Croft, Bryan Brzycki, Marta Burgay, Tobias Carozzi, Raimondo Concu, Daniel Czech, David DeBoer, Julia DeMarines, Jamie Drew, J. Emilio Enriquez, James Fawcett, Peter Gallagher, Michael Gerrert, Nectaria Gizani, Greg Hellbourg, Jamie Holder, Howard Isaacson, Sanjay Kudale, Brian Lacki, Matthew Lebofsky, Di Li, David H. E. MacMahon, Joe McCauley, Andrea Melis, Emilio Molinari, **Pearse Murphy**, Delphine Perrodin, Maura Pilia, Danny C. Price, Claire Webb, Dan Werthimer, David Williams, Pete Worden, Philippe Zarka, and Yunfan Gerry Zhang.  
“The Breakthrough Listen Search for Extraterrestrial Intelligence ”,  
*Astro2020: Decadal Survey on Astronomy and Astrophysics, APC white papers*, no. 223; *Bulletin of the American Astronomical Society*, Vol. 51, Issue 7, id. 223 (2019)

- 
5. David M. Long, **Pearse C. Murphy**, Georgina Graham, Eoin P. Carley, David Pérez-Suárez.  
“A Statistical Analysis of the Solar Phenomena Associated with Global EUV Waves”,  
*Solar Physics*, Volume 292 , Issue 185, (2017).

# Contents

<b>List of Publications</b>	<b>iii</b>
<b>List of Figures</b>	<b>vii</b>
<b>1 Introduction</b>	<b>1</b>
1.1 The Sun . . . . .	1
1.1.1 The Corona . . . . .	3
1.1.2 Solar Flares . . . . .	4
1.1.3 Coronal Mass Ejections (CMEs) . . . . .	5
1.2 Solar Radio Bursts . . . . .	6
1.2.1 Type III Bursts . . . . .	10
1.3 Low Frequency Radio Wave Scattering . . . . .	13
1.3.1 Source Sizes in the Corona . . . . .	13
1.4 Radio Interferometry . . . . .	13
1.4.1 Beam-forming . . . . .	16
1.5 Thesis Outline . . . . .	17
<b>2 Theoretical Background</b>	<b>19</b>
2.1 Introductory Concepts in Plasma Physics . . . . .	19
2.1.1 Plasma Frequency . . . . .	19
2.2 Radio Emission Mechanisms in the Solar Corona . . . . .	19
2.2.1 Bremstrahlung . . . . .	19
2.2.2 Gyroemission . . . . .	19
2.2.3 ECMI . . . . .	19
2.2.4 Plasma Emission . . . . .	19
2.3 Plasma Emission . . . . .	19
2.3.1 Generation of Langmuir Waves . . . . .	20
2.3.2 Wave-Wave Interaction . . . . .	22
<b>3 Instrumentation</b>	<b>25</b>
3.1 The LOw Frequency ARray (LOFAR) . . . . .	25
3.1.1 Antennas . . . . .	25
3.1.2 Digital Signal Pipeline . . . . .	25
3.1.3 RSP-CEP Beamlets . . . . .	25
3.1.4 TBB-CEP Packets . . . . .	25
3.2 The REALtime Transient Acquisition Backend (REALTA) . . . . .	25

---

3.2.1	Introduction . . . . .	26
3.2.2	REALTA . . . . .	30
3.2.2.1	Local networking . . . . .	30
3.2.2.2	Hardware description . . . . .	31
3.2.3	Software and pipelines . . . . .	33
3.2.3.1	Recording data . . . . .	35
3.2.3.2	Pre-processing data . . . . .	35
3.2.3.3	Pulsar and single pulse processing . . . . .	36
3.2.3.4	SETI data processing . . . . .	37
3.2.3.5	Future development and real-time analysis . . . . .	37
3.2.4	First results . . . . .	38
3.2.4.1	Pulsars . . . . .	40
3.2.4.2	Rotating radio transients . . . . .	42
3.2.4.3	Fast radio bursts . . . . .	44
3.2.4.4	Solar radio bursts . . . . .	45
3.2.4.5	Jovian auroral radio emission . . . . .	47
3.2.4.6	SETI . . . . .	50
3.2.5	Conclusions and future work . . . . .	53
<b>4</b>	<b>Measuring Source Sizes in Visibility Space</b>	<b>57</b>
4.1	Introduction . . . . .	57
4.2	Observation . . . . .	60
4.3	Data analysis and results . . . . .	61
4.3.1	Fitting the visibilities . . . . .	64
4.3.2	Type IIIb striae . . . . .	68
4.4	Discussion . . . . .	68
4.5	Conclusion . . . . .	71
<b>5</b>	<b>Scatterig Observations vs Theory</b>	<b>73</b>
<b>6</b>	<b>Future Work</b>	<b>75</b>
6.1	TBB data . . . . .	75
6.2	More Scattering . . . . .	75
	<b>References</b>	<b>77</b>

# List of Figures

1.1	Diagram of Sun's interior and atmospheric layers.	2
1.2	Model of electron density and temperature with height in the solar atmosphere.	3
1.3	GOES lightcurve for X9 class flare on 2017-09-10	5
1.4	CME observed with the LASCO C2 instrument on 2000-02-27. The blank area shows the extent of the coronagraph and the white circle represents the solar disk.	6
1.5	Cartoon of Type I-V radio bursts	7
1.6	A number of Type III bursts observed by Zucca et al. (2012) on 21 October 2011.	11
1.7	A two element interferometer	14
2.1	Langmuir wave distribution function and spectral energy density.	22
2.2	A three wave process of fundamental plasma emission $L \rightarrow T+S$	24
2.3	Three wave process of second harmonic plasma emission $L+L' \rightarrow T$	24
3.1	Aerial photograph of the Irish Low Frequency Array station IE613 (I-LOFAR) at Birr Castle, County Offaly.	27
3.2	Block diagram for REALTA and I-LOFAR.	33
3.3	System diagram for REALTA.	38
3.4	Sample of 19 pulsars observed with I-LOFAR and REALTA.	39
3.5	Overview of the sky positions of RRATs observed during RRAT census.	40
3.6	Observation of the Crab Pulsar performed on 30 June 2020.	43
3.7	Solar radio noise storm observed on 2 November 2020.	46
3.8	Two solar radio bursts observed on 2 June 2020.	48
3.9	Observation of a Jovian Decametric emission produced by the Io-Jupiter interaction.	49
3.10	Narrowband signal detected using REALTA and the turboSETI algorithm.	52
4.1	GOES X-ray lightcurves and dynamic spectrum for the duration of a LOFAR solar observation 2015-10-17.	62
4.2	Results of directly fitting LOFAR visibilities.	66
4.3	Recreated sky intensity profile of a Type IIIb radio burst	67



# Introduction

Since the first dawn of the Palaeolithic the sun has been a centre point of human life. Ancient passage tombs in Ireland and Western Europe are constructed in such a way that on the day of a solar solstice or equinox, they are illuminated throughout. While perhaps no longer as revered as by early humans, the sun is still a source of curiosity and finding our place in the universe. Not only are we dependent on the sun for light and heat, but are also in direct path of the explosive and energetic events such as coronal mass ejections and solar flares.

This chapter highlights some fundamental concepts of solar physics and how radio emission from the sun can be observed and the implications of its study.

## 1.1 The Sun

The Sun is our nearest star and the centre of our solar system however, apart from these distinctions it is a painfully average star. It is a G2 type star located squarely on the main sequence of the Hertzsprung Russell diagram. It has a luminosity of  $(3.84 \pm 0.04) \times 10^{26}$  W and a radius  $R_{\odot} = (6.959 \pm 0.007) \times 10^8$  m. The Sun's mass of  $(1.9889 \pm 0.0003) \times 10^{30}$  kg comprises  $> 99\%$  of the solar system's total mass ([Foukal, 2004](#)). At the time of writing the Sun is about halfway through it's  $\sim 10$  billion year life span. Formed from a cooling cloud of gas and dust 4.6 billion years ago, the Sun now has a core with a temperature of 15 MK, which enables nuclear fusion to occur and will continue to do so until its supply of Hydrogen runs out. At this point the Sun will start to fuse together Helium followed by progressively heavier elements until eventually the core will collapse and the resulting supernova will destroy any remains of life in the solar system.

## 1. INTRODUCTION

---

If one were to stop reading this thesis now they would be forgiven for thinking that there is nothing much interesting to be said about the Sun that distinguish it from other stars. However, given our proximity we are able to observe a vast array of phenomena, many of which have direct terrestrial impacts. These phenomena have their origins in the solar atmosphere and shall be described briefly below. It is important to point out that the study of these phenomena is inherently a study of the plasma and magnetic field structure of the solar atmosphere. The layer of the Sun at  $1 R_{\odot}$  is known as the photosphere and is what would be called the surface of the Sun. At this point, the mean free path of visible photons becomes much greater than the distance between the Sun and the Earth and can be thought as coming directly from the solar surface. Above the photosphere is the Sun's atmosphere consisting of the chromosphere, transition region and the corona.

### 1.1.1 The Chromosphere

### 1.1.2 The Transition Region

### 1.1.3 The Corona

The outermost layer of the solar atmosphere is called the corona. It is a hot, tenuous plasma which displays a number of interesting phenomena thought to be governed by its complex magnetic field. The corona begins  $\sim 2500$  km above the photosphere after a layer in the Sun's atmosphere known as the transition region, where electron density decreases and temperature increases dramatically (Figure 1.2). The electron density in the corona ranges from  $10^9 \text{ cm}^{-3}$  at the base to  $10^6 \text{ cm}^{-3}$  at distances of  $1 R_{\odot}$  from the solar surface. Densities vary throughout the corona. Sparse, underdense regions at the base of the corona known as coronal holes exhibit densities of  $\sim (0.5 - 1.0) \times 10^8 \text{ cm}^{-3}$  whereas areas of high magnetic activity known as active regions have electron densities

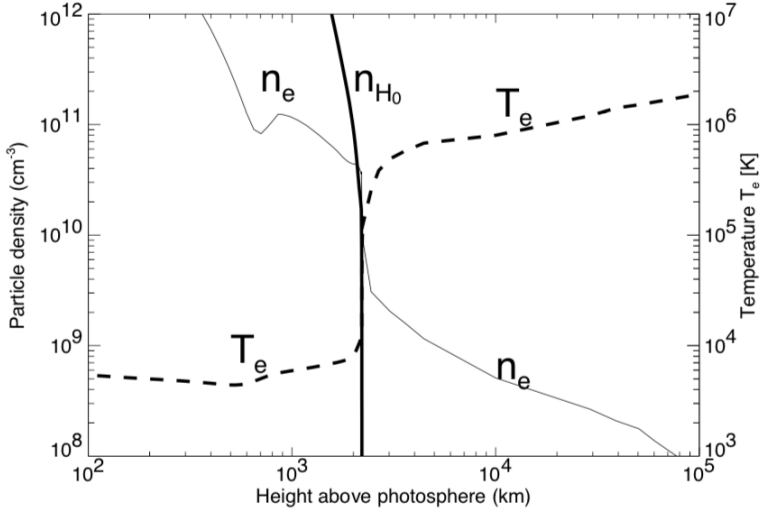


**Figure 1.1:** Model of electron density and temperature with height in the solar atmosphere. The region around 2000 km showing a sharp rise in temperature and sharp fall in electron density is known as the transition region, above this height plasma becomes fully ionised. Image taken from [Aschwanden \(2004\)](#)

of  $\sim 2 \times 10^9 \text{ cm}^{-3}$ .

Observing the white light corona is done with a number of ground-based and space-based instruments called coronographs, that emulate the effect of a total eclipse. The Large Angle and Spectrometric Coronagraph (LASCO) on board the Solar and Heliospheric Observatory (SOHO) is one such instrument and allows the corona to be observed from distances of  $2\text{-}32 R_\odot$ .

Energetic events in the corona such as solar flares and coronal mass ejections (CMEs), described in [1.1.2](#) and [1.1.3](#), are studied across the electromagnetic spectrum. They are studied in order to understand how particles are accelerated, how energy is released and ultimately, why the corona has such an unaccountably high temperature. Most particle acceleration events in the solar corona have a diagnostic in radio spectra. This PhD focuses on studying these radio diagnostics at their highest temporal and spatial resolutions to date.

## 1. INTRODUCTION

---

### 1.1.4 Solar Flares

Solar flares are massive releases of magnetic energy commonly believed to be due to a reconfiguration in the complicated magnetic field structure in an active region. They are some of the most energetic events in the solar system, releasing  $\sim 10^{25}$  J of energy over a matter of minutes. Flares are observed across the electromagnetic spectrum from radio waves to  $\gamma$  rays with energies  $> 10$  MeV. They are classified by the amount of X-ray flux ( $\text{W m}^{-2}$ ) detected by the Geostationary Operational Environmental Satellite (GOES) 1-8 Å band on a logarithmic scale as being A, B, C, M or X class with A being the lowest flux ( $10^{-8} \text{ W m}^{-2}$ ) and X the highest ( $10^{-4} \text{ W m}^{-2}$ ). Each class is further subdivided into a linear scale. A timeseries of X-ray flux from a solar flare is often called a lightcurve and has three characteristic phases; a pre-flare phase which shows X-ray flux associated with the active region where the flare occurs, an impulsive phase showing a sharp rise in X-ray flux corresponding to accelerated particles colliding with the solar surface, and a gradual decay phase where plasma heated by the flare gradually cools back to its pre-flare state. Figure 1.3 shows a GOES light curve of the X9 class flare that occurred on 2017-09-10 and the three flare phases described above.

During solar flares, magnetic structures known as coronal loops fill with hot plasma and begin to emit in soft X-rays. At the same time, electrons are accelerated towards the solar surface where their energy is converted to hard X-rays in the collision via bremsstrahlung.

### 1.1.5 Coronal Mass Ejections (CMEs)

In certain magnetic reconnection events, plasma suspended in a magnetic flux rope erupts from the corona into the heliosphere, the volume around the Sun where the interplanetary medium is dominated by particles flowing outward from the Sun. These eruption events are known as coronal mass ejections and accelerate  $10^{15}$  g of charged

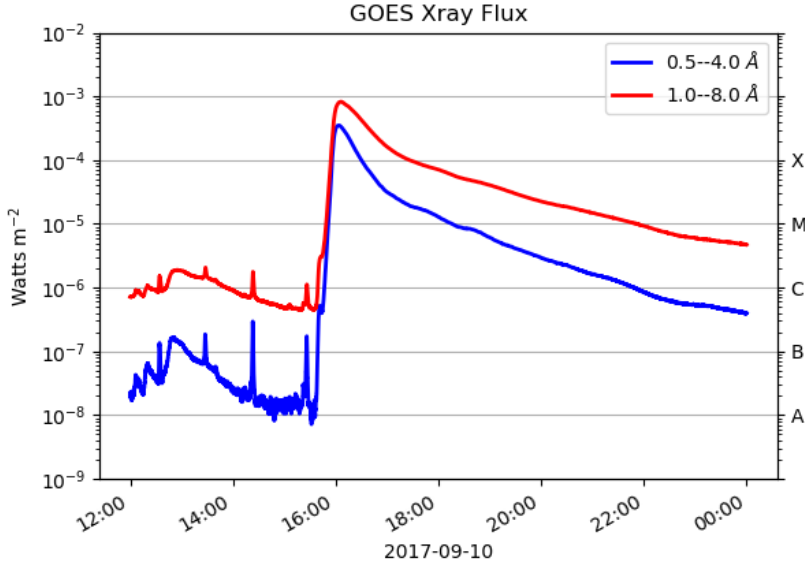


**Figure 1.2:** The GOES lightcurve of the X9 flare that occurred on 2017-09-10. The red curve shows the 1-8 Å channel by which the flare is classified while the blue curve shows the 0.5-4 Å band. The three characteristic phases of a solar flare are clearly displayed here. The pre-flare phase before  $\sim 16 : 00$  UTC, the impulsive phase indicated by the sharp rise in flux and the gradual decay phase where X-ray flux gradually returns to the pre-flare level.

particles at typical speeds of up to  $\sim 2500 \text{ km s}^{-1}$  ([Gopalswamy & Thompson, 2000](#)).

A “textbook” CME structure consists of a bright front that surrounds a dark cavity and a bright central core. CMEs are observed using coronagraphs as they are much fainter than the solar disk. An example of a CME observed using the LASCO C2 corona with a field of view from  $1.5 R_{\odot}$  to  $6 R_{\odot}$  can be seen in Figure 1.4. Ejected material from a CME can interact with the Earth’s magnetosphere and are known to have caused adverse effects including satellite communication disruption, radio blackouts, wide spread power outages and large inaccuracies in GPS postions. CMEs can travel faster than local Alfvén speed in the corona leading to a shock which can accelerate particles.

## 1. INTRODUCTION

---

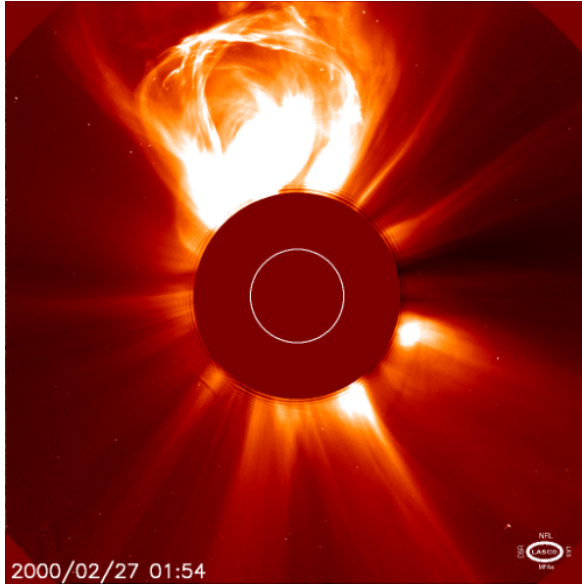


**Figure 1.3:** CME observed with the LASCO C2 instrument on 2000-02-27. The blank area shows the extent of the coronagraph and the white circle represents the solar disk.

## 1.2 Solar Radio Bursts

Particles in the solar corona are accelerated by solar flares and CMEs, resulting in a range of radio bursts distinguish in spectra as the “classic” Type I-V radio bursts described by Wild (1950). A wealth of other fine structure radio bursts are also observed, predominantly found in radio storms such as S bursts, drift pairs and stria (McConnell, 1980; Melrose, 1982; Nelson & Melrose, 1985). The fine structure of these bursts can often reveal information about small-scale turbulence in the corona (Kontar et al., 2017) and offer the greatest chance of solving the coronal heating problem.

A brief description of some solar radio phenomena is given here while a more in depth review of the plasma emission process is given in appendix ??.

**Type I bursts** Type I emission can appear as bursts and/or a continuum originating from “storm centres” that are associated with active regions. Type I storms can last for many days. Emission from Type I bursts is highly circularly polarised in the o-mode

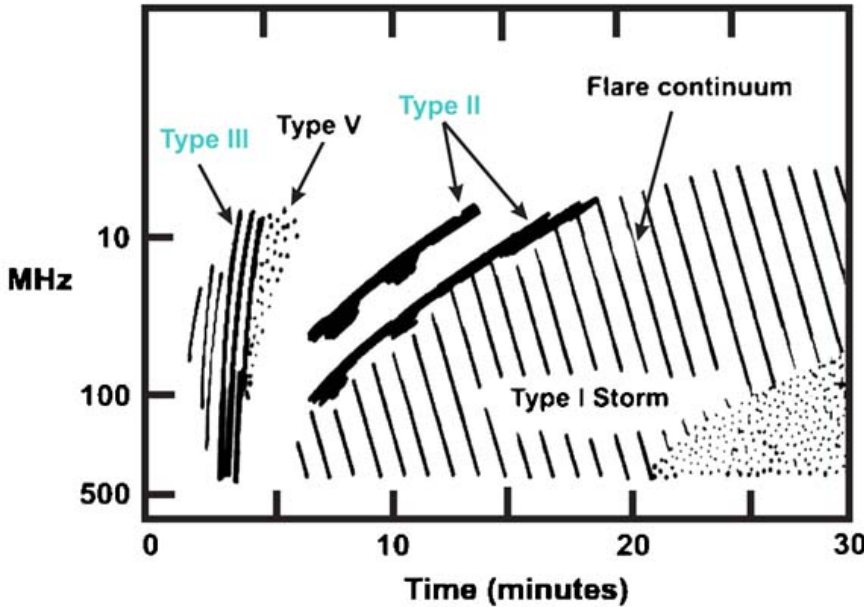


**Figure 1.4:** A cartoon of Type I-V radio bursts. Image taken from [Cliver & Ling \(2009\)](#)

(whereby light is circularly polarised in the same direction as electrons gyrating about a magnetic field line) and is also particularly directional with an increase in intensity as active regions rotate to the centre of the disk. Unlike Type II or III bursts, they do not exhibit a harmonic structure.

**Type II bursts** Type II radio bursts are a form of radio emission seen from the Sun and are identified by a slow ( $\sim 0.1 \text{ MHz s}^{-1}$ ) drift to lower frequencies in dynamic spectra. The frequency drift can be used to find the velocity of the shock causing a burst if the electron number density as a function of height is known. The velocities of Type II bursts are often found to be  $\sim 1000 \text{ km s}^{-1}$ , much faster than the Alfvén velocity in the quiet corona,  $\approx 270 \text{ km s}^{-1}$ , meaning a shock must be present. Other basic properties of Type II bursts include:

1. Narrow bandwidths of up to  $\sim 100 \text{ MHz}$  from initial to final frequencies.
2. A harmonic structure of two bands with a frequency ratio slightly less than 2:1 at a fundamental,  $f_p$ , and harmonic,  $2f_p$ , frequency can be seen for most Type

## 1. INTRODUCTION

---

II bursts. This structure is consistent with the idea that Type II emission is due to plasma oscillations.

3. A large number of Type II bursts contain band splitting into an upper and lower band for each of the harmonics in their spectra. The cause for this splitting is not fully understood but it is commonly thought that the two bands are related to emission upstream and downstream of the MHD shock front which causes the Type II burst ([Nelson & Melrose, 1985](#); [Smerd et al., 1974](#); [Vršnak et al., 2002](#)).
4. Herringbone structure. Approximately 20% of Type II bursts show a herringbone structure of rapidly drifting emission spikes shooting out of the “backbone” of the main frequency drift to higher and lower frequencies. These herringbones are thought to be due to electron beams being accelerated at the associated shock for the Type II burst ([Mann, 1995](#)). While the backbone is poorly polarised, the herringbones have been found to be quite strongly,  $\sim 70\%$ , polarised. This is further evidence that herringbone structure is due to Type III-like emission from accelerated electron beams.
5. Starting emission frequencies of the order of a few 100 MHz ending at frequencies above 20 MHz. This being said, Type II burst with starting frequencies of  $\sim 100$  kHz have also been observed. These lower frequency bursts are thought to be due to interplanetary shocks whereas higher frequency bursts are considered to be from shocks in the low corona.
6. Typical durations of 5-15 minutes. Type II bursts that occur after a flare do so with a delay ranging from 2-20 minutes. Bursts with shorter durations generally have higher starting frequencies.

Based on these and a number of other properties discussed in greater detail by [Nelson & Melrose \(1985\)](#), Type II radio bursts can be used as indicators for MHD

shocks in the solar corona. Observational proof of frequency varying inversely with time in the solar wind, consistent with radiation being generated at  $f_p$  and  $2f_p$  directly upstream from a CME-driven shock, was found by [Reiner et al. \(1997\)](#) and solidifies this argument.

**Type IV burst** Type IV bursts come in at least three sub-types with the general characteristic that they are of the form of broadband emission lasting for several hours. Early stationary Type IV bursts (also known as the flare continuum) associated with the decay phase of solar flares, late stationary bursts which appear similar to Type I emission, and moving Type IV bursts which exhibit a smooth, wide-band spectrum.

**Type V burst** The last of the broadband emission bursts, Type V radio bursts typically have a duration of 1-3 minutes and appear as an afterglow from Type III bursts. Type V emission is strictly less than 150 MHz and is accepted that it results from electrons that generate a Type III burst and become trapped in a closed magnetic loop in the corona.

**Fine Structure: S bursts** S bursts, initially called Fast Drift Storm (FDS) bursts, were first observed at the Culgoora Solar Observatory in 1967 ([Ellis, 1969](#)) They were later renamed by [McConnell \(1980\)](#) who likened them to Jovian S bursts. They have a narrow bandwidth of the order of 0.03 MHz and a drift rate of  $1\text{-}2 \text{ MHz s}^{-1}$  and durations much less than 1s. [McConnell \(1980\)](#) also concluded that S bursts are radiated at either the plasma frequency or its harmonic in a manner similar to Type III bursts, see appendix ??, but that the implications of S burst fine structure and coronal scattering can only be defined once it is determined which harmonic of the plasma frequency they are radiated at. [Melnik et al. \(2010a\)](#) propose a model of S bursts being generated by coalescence of fast magnetosonic waves with Langmuir waves which agrees well with the analysis of [Clarke et al. \(2019\)](#). Modern observations of

## 1. INTRODUCTION

---

S bursts, such as those conducted using LOFAR’s tied-array imaging mode ([Morosan et al., 2015](#)), can give greater insight into the spectral and temporal variability of S bursts and what this might mean for the environment they are generated in.

### 1.2.1 Type III Bursts

Type III bursts are possibly the most useful radio burst for studying various aspects of the corona outlined later. Furthermore, section ?? describes a Type III burst that is being analysed as part of this PhD. [Reid & Ratcliffe \(2014\)](#) review a number of notable properties of Type III bursts. The defining characteristic of Type III bursts is a drift from high to low frequencies in a dynamic spectrum. The drift rates for Type III bursts are typically quite fast, of the order of  $\sim 10 \text{ MHz s}^{-1}$  depending on the frequency. The frequency drift rate,  $df/dt$ , has been found to have various relations with frequency ([Reid & Ratcliffe, 2014](#)) but most agree that  $df/dt \propto f^\alpha$ , where  $\alpha$  varies depending on the study from  $\sim 1$  to  $\sim 2.7$ .

[Ginzburg & Zhelezniakov \(1958\)](#) proposed that Type III bursts are emitted at the plasma frequency,

$$\omega_p^2 = \frac{n_e e^2}{m_e \varepsilon_0} \quad (1.1)$$

where  $n_e$  is the number density of electrons,  $m_e$  is the electron mass,  $e$  is the electron charge and  $\varepsilon_0$  is the permittivity of free space. Although Eq. 1.1 is relatively simple, it contains an important principle of plasma physics. Namely, the plasma frequency is proportional to the square root of the electron density. This means that plasmas at higher electron densities will oscillate at higher frequencies than those of lower densities. The drift in Type III bursts, which are emitted at  $\omega_p$ , is therefore an indication of the emission source moving from an area of high electron density, the photosphere, to low density, the upper corona.

Type III bursts are observed to be in two bands, a fundamental and harmonic

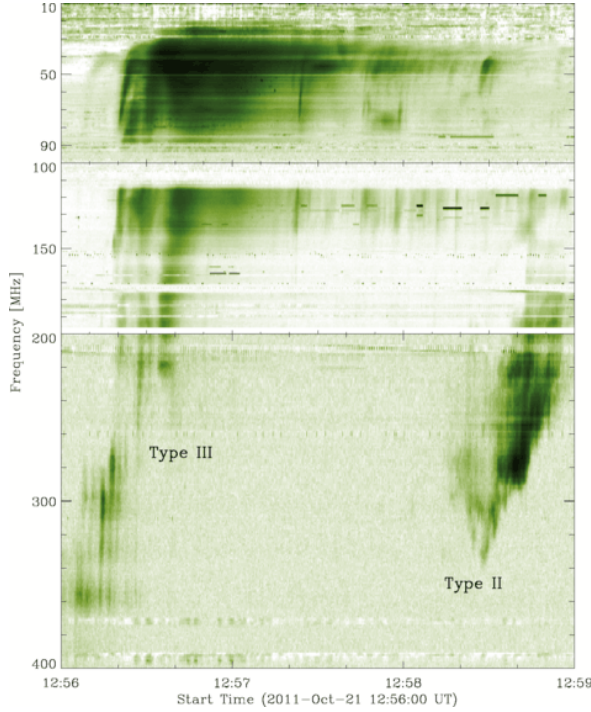


**Figure 1.5:** A number of Type III bursts observed by [Zucca et al. \(2012\)](#) on 21 October 2011. Note the Type III storm below 200 MHz and the Type II burst between 140 and 330 MHz.

band that are emitted at  $\omega_p$  and  $2\omega_p$  respectively. Both bands exhibit the same frequency drift although the flux of the harmonic band is usually less than that of the fundamental band. The process of plasma emitting radio frequencies at  $\omega_p$  and  $2\omega_p$  will be explained in more detail in section 2.3.2.

Figure 1.6 shows Type III radio bursts below 400 MHz observed by [Zucca et al. \(2012\)](#). A Type II burst was also observed between 140 and 330 MHz and exhibits a much slower frequency drift than the Type III bursts. A Type III storm can be seen below 200 MHz. This is when Type III emission is continuous over the span of large time scales and can last days. Type III bursts come in a number of subcategories described below.

**Reverse and bi-directional bursts** A typical Type III burst is produced when an electron beam travels along a magnetic field line away from the Sun to areas of lower density. During the magnetic reconnection process that accelerates these electrons,

## 1. INTRODUCTION

---

some electrons travel towards the Sun to areas of higher density and thus have a reversed frequency drift. Bursts where both the regular and reverse drifts can be seen simultaneously are bi-directional bursts.

**Type IIIb bursts** While typical Type III bursts have smooth emission, Type IIIb bursts contain a fragmented substructure. This substructure is in the form of a chain of emission bands/striae that drift in frequency as a whole but individually show little frequency drift.

**Type U and J bursts** In the case where electrons are travelling along a closed magnetic field line, a turning point in the frequency drift of a Type III burst can be observed. For electrons that generate radio emission down to the footpoint of the magnetic field line, a U burst is observed. A U burst can be identified as an inverted U on a dynamic spectrum. More often, electrons stop generating radio emission as they travel back down the magnetic field line so only the turning point in frequency drift is visible in dynamic spectra. These are known as J type bursts. The reason for higher occurrence of J bursts compared to U bursts is described by [Reid & Kontar \(2017\)](#).

## 1.3 Low Frequency Radio Wave Scattering

### 1.3.1 Source Sizes in the Corona

Analysis of short temporal bursts with small bandwidths suggest source sizes in the corona to be of the order  $\sim 6000$  km ([McConnell, 1980](#)). Radio images of the Sun at metric and decametric wavelengths have yet to reveal this level of spatial structure. This is mostly due to the limit of resolution obtainable with modern interferometers however, the suggestion that there is a fundamental limit imposed upon the level of

resolution obtainable by scattering in a turbulent corona ([Bastian, 1994](#)) has gathered a following in recent years ([Kontar et al., 2017](#)). [Riddle \(1974\)](#) described the effect of scattering in a spherically symmetric corona with random isotropic inhomogeneities with and without density enhancements due to streamers. Here they showed that the “directivity pattern”, the ratio of the power received from a source with and without scattering, was significantly broadened for radio bursts near the local plasma frequency, 80 MHz in their case. Sub-arcminute interferometric observations of Type III radio bursts could give a definitive answer to this question.

## 1.4 Radio Interferometry

There are two limiting factors in modern-day optical astronomy, diffraction and atmospheric conditions. The latter has been overcome using advanced adaptive optics techniques or avoided entirely by putting telescopes in space. This leaves diffraction as a fundamental limit to the resolving power of any telescope.

Rayleigh’s criterion states that for an object to be resolved, the maximum of its interference pattern must overlap the minimum of another. This leads to the mathematical relationship (assuming a circular aperture),

$$\theta \approx 1.22 \frac{\lambda}{D}$$

where  $\theta$  is the angular resolution of an object,  $\lambda$  is the wavelength observed in and  $D$  is the aperture diameter of the telescope. The Hubble Space Telescope, with a diameter of 2.4 m and observing in near IR therefore has an angular resolution of  $\sim 0.05$  arcseconds. For a radio telescope observing 10 m waves to have the same resolution, ignoring atmospheric effects, it would need an aperture diameter of 41000 km. Building a single dish of this size is practically impossible. Fortunately, because radio waves

## 1. INTRODUCTION

---

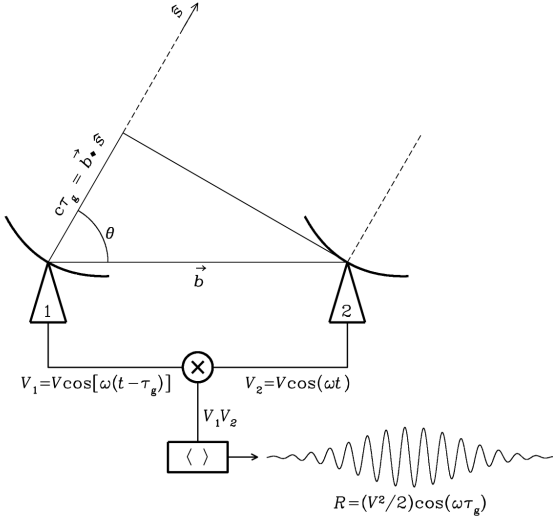


**Figure 1.6:** A two element interferometer separated by a baseline  $\vec{b}$ . The signal from each antenna is correlated by first multiplying the two voltages then time averaging them.

are so large, they can be detected at multiple locations at great distances from each other and the original signal pieced back together. This idea forms the basis of radio interferometry. The mathematical framework for this is *slightly* more complicated than this simple view so to explain it the most fundamental radio interferometer, the two element interferometer, is described.

Consider two radio antennae, 1 and 2, separated by a distance  $\vec{b}$ , this is the antenna baseline and is equivalent to the diameter of a classic telescope. A radio wave approaching the antennae from direction  $\hat{s}$  will hit antenna 2 first then antenna 1 after a time delay of  $\tau_g$  such that,

$$\tau_g = \frac{\vec{b} \cdot \hat{s}}{c}$$

where  $c$  is the speed of light. The output from each antenna is a voltage  $V_1 = V \cos \omega(t - \tau_g)$  and  $V_2 = V \cos \omega t$ . The total response,  $R_c$  of the interferometer is the correlation or multiplication and time average of these two voltages,  $\langle V_1 V_2 \rangle$ .

$$R_c = \langle V_1 V_2 \rangle = \frac{V^2}{2} \cos \omega \tau_g$$

Furthermore, if a  $90^\circ$  phase shift is added to the output of one antenna, the response becomes

$$R_s = \langle V_1 V_2 \rangle = \frac{V^2}{2} \sin \omega \tau_g$$

A complex visibility can be defined as the complex sum of the two responses  $V(\hat{\mathbf{s}}) = R_c - iR_s$ . Using Euler's formula, the complex visibility of an extended source is given by:

$$V(\hat{\mathbf{s}}) = \int I(\hat{\mathbf{s}}) \exp(-i\omega \tau_g) d\Omega = \int I(\hat{\mathbf{s}}) \exp(-2\pi i \frac{\vec{\mathbf{b}} \cdot \hat{\mathbf{s}}}{\lambda}) d\Omega \quad (1.2)$$

where  $I$  is the sky brightness distribution. In more conceptual terms, the complex visibility is the Fourier transform of the sky brightness distribution.

Equation 1.2 can be rewritten as a function of the  $uvw$  coordinate system and using the directional cosine coordinate system for source position on the sky.

$$V(u, v) = \int I(l, m) \exp(-2\pi i(ul + vm)) dl dm \quad (1.3)$$

The coordinate system commonly used throughout radio interferometer is the  $l, m, n$  or directional cosine coordinate system. This determines a position on the sky in terms of the direction cosines to that position. Here  $l, m, n$  are defined as

$$l = \cos \delta \sin \Delta \alpha, \quad m = \sin \delta \cos \delta_0 - \cos \delta \sin \delta_0 \cos \Delta \alpha, \quad n = \sqrt{1 - l^2 - m^2}$$

where  $\delta, \delta_0$  are the declinations of an object and the phase centre, respectively, and  $\Delta \alpha = \alpha - \alpha_0$  is the difference between the right ascension of the object and phase centre (direction of the primary beam).

Baselines in radio interferometry are described using the  $uvw$  coordinate system

## 1. INTRODUCTION

---

defined as

$$\begin{bmatrix} u \\ v \\ w \end{bmatrix} = \frac{1}{\lambda} \begin{bmatrix} \sin H & \cos H & 0 \\ -\sin \delta \cos H & \sin \delta \sin H & \cos \delta \\ \cos \delta \cos H & -\cos \delta \sin H & \sin \delta \end{bmatrix} \begin{bmatrix} B_x \\ B_y \\ B_z \end{bmatrix}$$

Here,  $H$  is the hour angle of an object,  $\delta$  is its declination,  $\mathbf{B} = (B_x, B_y, B_z) = (x_2 - x_1, y_2 - y_1, z_2 - z_1)$  is the baseline or distance between two antennae and  $\lambda$  is the wavelength of the radio waves being observed.

### 1.4.1 Beam-forming

In its most simple terms, beamforming means pointing a phased array in a particular direction. It involves correcting for phase difference between the “phase centre” of the beam and the position of the source of interest for each baseline and then summing it all together. In order to beamform, one must account for the phase difference between the phase centre (where the beam is physically pointing) and the source (at an angular coordinate of  $(l, m)$  with reference to the phase centre). As above, this phase difference for a baseline  $pq$  is given by,

$$\kappa_{pq} = 2\pi(u_{pq}l + v_{pq}m + w_{pq}(n - 1))$$

In order to correct for the phase difference and steer the beam, data for baseline  $pq$  is multiplied by the complex weight  $e^{-i\kappa_{pq}}$ , this is repeated for all baselines and finally all data is summed.

## 1.5 Thesis Outline

The high spatial, temporal and spectral resolution of modern radio interferometers such as LOFAR and the launch of new space missions including Parker Solar Probe

and Solar Orbiter has ushered in a new age of solar radio observations. By developing computational hardware and using a unique fitting method, this thesis has furthered the capability of an international LOFAR station and interferometric observations. This thesis outlines how such developments have improved our knowledge of the solar corona at some of the smallest scales ever measured. In Chapter 2 I outline the relevant background theory for the work presented in this thesis. Chapter 3 will describe the instrumentation and data processing facility used for this work.

The study of radio wave scattering in the solar corona has undergone a renaissance in recent years both in terms of computational modelling and observations. Chapter 4 will describe how, for the first time, LOFAR visibilities were fitted directly to estimate the root mean squared fluctuations of electron density in the solar corona, the key parameter in any scattering studies. In order to accurately compare between models of the solar corona, I present over 100 radio bursts and determine their size and position in Chapter 5.

Chapter 6 includes a discussion on the future work that can be carried out from the foundations of this thesis. It outlines the necessary further studies needed to further our knowledge of radio wave scattering even further and how to utilise even higher temporal resolution observations of the radio sun. Chapter 6 will also contain a summary and conclusion of the work presented in this thesis.

## 1. INTRODUCTION

# Theoretical Background

The following chapter describes the core concepts relevant to this thesis in more detail than Chapter 1. Here I discuss the various mechanisms for radio wave emission in the solar corona, with particular emphasis on the plasma emission process. I will also give an introduction to the mathematical formalisms of radio interferometry.

## 2.1 Introductory Concepts in Plasma Physics

Plasma was the name given by Langmuir to the new, exotic type of matter he was studying in the 1920s. It is essentially an ionized gas that exhibits quasi-neutrality on a macroscopic scale. Maxwell-Boltzman distributions.

### 2.1.1 Plasma Frequency

## 2.2 Radio Emission Mechanisms in the Solar Corona

### 2.2.1 Bremstrahlung

### 2.2.2 Gyroemission

### 2.2.3 ECMI

### 2.2.4 Plasma Emission

## 2.3 Plasma Emission

In 1942 while Britain was on the look out for radar signals of enemy aircraft, a strong, noise like and highly variable signal was noticed by radar operators. Initially it was

## 2. THEORETICAL BACKGROUND

---

thought that Germany had managed to learn the secret of radar and create some sort of jamming device. On further investigation it was found that this jamming was in fact radio emission from the Sun. The discovery of this radio emission being associated with a major solar flare was kept secret until after the war and was published by [Appleton & Hey \(1946\)](#). Since then a number of major advancements in both instrumentation and theory have occurred. A culmination of the theory of solar radio emission is laid out in the book by [McLean & Labrum \(1985\)](#) while worldwide, a number of extraordinary radio telescopes and interferometers such as the LOw Frequency ARray (LOFAR, [van Haarlem et al., 2013](#)), the Nançay Radio Heliograph and the Murchison Widefield Array (MWA), to name but a few, have been built.

Solar radio emission often comes in the form of bursts of varying timescales. These were initially classified into three types by [Wild & McCready \(1950\)](#) with a fourth and fifth type being discovered by [Boischot & André \(1957\)](#) and [Wild et al. \(1959\)](#) respectively. Of these, the most frequently occurring are the so called Type III radio bursts. These are short bursts that can be observed over many frequencies and are found to be associated with solar flares ([Malville & M., 1962](#)). An initial study into how they are emitted was conducted by [Ginzburg & Zhelezniakov \(1958\)](#).

For a Type III radio burst to be emitted, an electron must generate Langmuir waves in the plasma. These Langmuir waves then go on to generate electromagnetic transverse waves by coalescing with other waves or by decaying. These electromagnetic waves are the radio bursts that are observed. In this section the generation of Langmuir waves and the process of plasma emission are discussed.

### 2.3.1 Generation of Langmuir Waves

During magnetic reconnection in a solar flare electrons are accelerated along magnetic field lines. As these beams of electrons propagate, faster electrons begin to outpace

slower electrons and stationary ions in the background plasma. This leads to a second peak on the Maxwell Boltzmann distribution of velocities as seen in Figure 2.1. Energy is transferred from electrons electrons travelling at the phase velocity,  $v_\phi$ , to Langmuir waves creating a resonance. The positive velocity gradient of this resonance means that there are more electrons with velocity greater than  $v_\phi$  than there are electrons with velocities less than  $v_\phi$  (where energy is transferred from the wave to the particles), this causes Langmuir waves to become unstable and their magnitudes to grow exponentially. Particles with velocities near  $v_\phi$  are in resonance with the Langmuir waves and drive this instability.

This instability is alleviated by what is known as quasi-linear relaxation (Melrose, 1987) whereby the resonant behaviour of the electrons and Langmuir waves results in a plateau in the Maxwell Boltzmann distribution rather than a second peak. It can be shown that (Vedenov, 1963) the electron distribution function,  $f(v, t)$  where  $\int f(v, t)dv = n_e$ , and the spectral energy index of Langmuir waves,  $W(v, t)$  such that  $\int W(v, t)dv = E_L$  the total energy density, can be expressed as follows (Reid & Ratcliffe, 2014),

$$\frac{\partial f(v, t)}{\partial t} = \frac{4\pi^2 e^2}{m_e^2} \frac{\partial}{\partial v} \left( \frac{W}{v} \right) \frac{\partial f(v, t)}{\partial v} \quad (2.1)$$

$$\frac{\partial W(v, t)}{\partial t} = \frac{\pi \omega_p}{n_e} v^2 W \frac{\partial f(v, t)}{\partial v} \quad (2.2)$$

Equation 2.2 shows that the growth rate of Langmuir waves is proportional to  $\frac{\partial f(v, t)}{\partial v}$ , hence a positive gradient in the Maxwell Boltzmann distribution leads to a growth in Langmuir waves. The right hand side of Eq. 2.1 has a diffusion operator  $D = \frac{W}{v}$ . This states that the transfer of energy from particles to waves and back leads to the distribution function being smoothed out and eventually becoming a plateau. The evolution of  $f(v, t)$  and  $W(v, t)$  with time is shown in Figure 2.1. Figure 2.1 shows how the plateau in the distribution function and a broadening in the spectral energy

## 2. THEORETICAL BACKGROUND

---

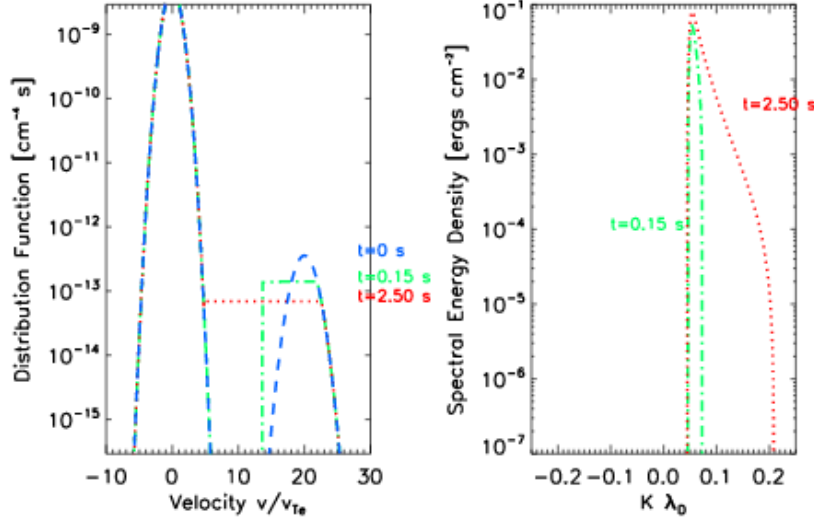


**Figure 2.1:** Left: Evolution of distribution function (normalised by the electron thermal velocity  $v_{Te} = V_e$ ) in time. The diffusive term in 2.1 causes the bump-on-tail Gaussian to turn into a plateau, thereby eliminating the instability caused by the positive velocity gradient. Right: The spectral energy density of generated Langmuir waves, x-axis normalised to the Debye length  $\lambda_D = \sqrt{\frac{\epsilon_0 k_B T_e}{e^2 n_e}}$ . As time passes the spectral range of Langmuir waves increases. Each panel shows successive times of  $t=0.15$ s (green, dot-dashed line) and  $t=2.50$ s (red, dotted line). (Figure taken from [Reid & Ratcliffe, 2014](#)).

density develop as time progresses.

### 2.3.2 Wave-Wave Interaction

Wave-wave interaction concerns the processes by which three types of waves interact. These are: transverse (T) waves, Langmuir (L) waves and ion sound (S) waves, and have the following, respective dispersion relations,

$$\omega = (\omega_p^2 + k^2 c^2)^{\frac{1}{2}}$$

$$\omega \cong \omega_p + \frac{3k^2 V_e^2}{2\omega_p}$$

$$\omega = kv_s$$

where  $V_e$  is the thermal velocity of electrons in the plasma,  $v_s$  is the ion sound speed and  $k$  is the wave vector. Only transverse waves with  $\omega > \omega_p$  can escape and thus a plasma emission mechanism is a process that generates these transverse waves.

As mentioned in Section 1.2.1, Type III bursts have a harmonic structure associated with plasma emission at the plasma frequency and the second harmonic. Both of these transverse waves are formed in different three wave processes that will now be discussed. In a plasma, due to scattering from other wave modes and ions in the plasma, a wave mode can be changed from one to the other. This is expressed in the equation

$$\sigma \rightleftharpoons \sigma' + \sigma''$$

where  $\sigma$ ,  $\sigma'$  and  $\sigma''$  represent different wave modes. Conservation of energy and momentum state,

$$\omega^\sigma(k) = \omega^{\sigma'}(k') + \omega^{\sigma''}(k'')$$

$$k = k' + k''$$

where  $\omega^\sigma(k)$  is the frequency of a particular wave mode with the wave vector  $k$ . For Langmuir (L), ion sound (S) and transverse (T) wave modes the allowed processes are  $L+S \rightarrow L'$ ,  $L+S \rightarrow T$ ,  $T+S \rightarrow L$ ,  $T+S \rightarrow T'$  and  $L+L' \rightarrow T$ . Of these  $L+S \rightarrow T$ ,  $L \rightarrow T+S$  are responsible for fundamental emission while harmonic emission is associated with the three wave process  $L+L' \rightarrow T$ .

Originally [Ginzburg & Zhelezniakov \(1958\)](#) considered fundamental emission to be due to Langmuir waves scattering off of thermal ions in the plasma. It is now commonly accepted that the biggest cause of fundamental emission is due to the three wave processes of a Langmuir wave coalescing with an ion sound wave generated by  $L \rightarrow L'+S$  or when a Langmuir wave decays into an ion sound wave and an electromagnetic transverse wave. The process  $L \rightarrow T+S$  can be visualised as in Figure 2.2. In solar

## 2. THEORETICAL BACKGROUND

---

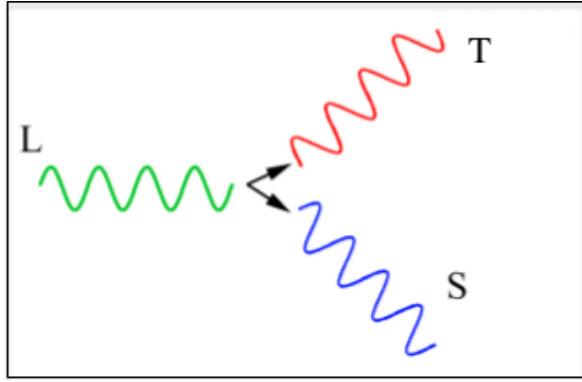


**Figure 2.2:** A three wave process of fundamental plasma emission  $L \rightarrow T + S$ . A Langmuir wave decaying into an ion sound wave and an electromagnetic transverse wave at the plasma frequency. (Figure adapted from Solar (interplanetary) Radio Bursts: the Generation of Radio Waves, an oral presentation by David Malaspina at the Jean Louis Steinberg International Workshop on Solar, Heliospheric and Magnetospheric Radioastronomy, November 2017)

radio physics it is often assumed that  $k_L \gg k_T$ , knowing this and that the wave vectors must satisfy  $\mathbf{k}_L \pm \mathbf{k}_s = \mathbf{k}_T$  (+ for  $L+S \rightarrow T$ , - for  $L \rightarrow T+S$ ) implies  $\mathbf{k}_s \approx \mp \mathbf{k}_L$

Second harmonic emission occurs when two Langmuir waves coalesce in the process  $L+L' \rightarrow T$ , shown in Figure 2.3. Conservation of momentum requires that  $\mathbf{k}_L + \mathbf{k}'_L = \mathbf{k}_T$  and for second harmonic (H) generation,  $k_T = k_H \approx \frac{\sqrt{3}\omega_p}{c}$ . The phase speed  $v_\phi$  of Langmuir waves is much less than  $\frac{c}{\sqrt{3}}$  meaning that  $k_L \gg k_T$  which results in  $\mathbf{k}_L \approx -\mathbf{k}'_L$ . This means that for a transverse wave at the second harmonic to be created, two Langmuir waves must coalesce almost exactly head on. These backward propagating Langmuir waves are generated: in the three wave processes of  $L+S \rightarrow L'$  and  $L \rightarrow L'+S$ ; scattering off of thermal ions; and refraction at density inhomogeneities.

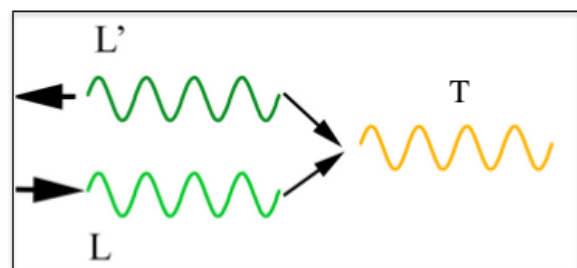


**Figure 2.3:** Three wave process of second harmonic plasma emission  $L+L' \rightarrow T$ . A Langmuir wave ( $L$ ) and a backwards propagating Langmuir wave ( $L'$ ) coalesce to form a transverse wave ( $T$ ) at  $2\omega_p$ . (Figure adapted from Solar (interplanetary) Radio Bursts: the Generation of Radio Waves, an oral presentation by David Malaspina at the Jean Louis Steinberg International Workshop on Solar, Heliospheric and Magnetospheric Radioastronomy, November 2017)

## 2. THEORETICAL BACKGROUND

# Instrumentation

This chapter describes the instrumentation used throughout the work for this thesis including a detailed description of the signal processing pipeline of an international LOFAR station such as I-LOFAR. Here I also describe the REALtime Transient Acquisition Backend (REALTA) that was developed over the course of this work.

## 3.1 The LOW Frequency ARray (LOFAR)

### 3.1.1 Antennas

### 3.1.2 Digital Signal Pipeline

### 3.1.3 RSP-CEP Beamlets

### 3.1.4 TBB-CEP Packets

## 3.2 The REALtime Transient Acquisition Backend (REALTA)

Modern radio interferometers such as the LOW Frequency ARray (LOFAR) are capable of producing data at hundreds of gigabits to terabits per second. This high data rate makes the analysis of radio data cumbersome and computationally expensive. While high performance computing facilities exist for large national and international facilities, that may not be the case for instruments operated by a single institution or a small consortium. Data rates for next generation radio telescopes are set to eclipse those currently in operation, hence local processing of data will become all the more important. Here, we introduce the REAL-time Transient Acquisition backend

### 3. INSTRUMENTATION

---

(REALTA), a computing backend at the Irish LOFAR station (I-LOFAR) which facilitates the recording of data in near real-time and post-processing. We also present first searches and scientific results of a number of radio phenomena observed by I-LOFAR and REALTA, including pulsars, fast radio bursts (FRBs), rotating radio transients (RRATs), the search for extraterrestrial intelligence (SETI), Jupiter, and the Sun.

#### 3.2.1 Introduction

Modern radio interferometers produce more data than any astronomical instrument in history. Interferometric observations can receive data at hundreds of gigabits per second, requiring high performance computer (HPC) facilities to preprocess data before it can be analysed and scientifically explored. With newly built telescopes such as the Murchison Widefield Array (MWA; [Lonsdale et al., 2009](#)), MeerKAT ([Jonas, 2018](#)) and the Australian Square Kilometre Array Pathfinder (ASKAP; [Johnston et al., 2008](#)) acquiring such vast amounts of data (up to 300 Gbps; [Lonsdale et al., 2009](#); [Voronkov, 2020](#)) radio astronomy is working at the cutting edges of big data science. The Square Kilometre Array ([McMullin et al., 2020](#)) is commencing construction this year and pushes the computational requirements to ever more difficult regimes ([Scaife, 2020](#)).

The LOw Frequency ARray (LOFAR; [van Haarlem et al., 2013](#)) is a radio interferometer located in eight countries across Europe. The majority of the LOFAR stations exist in a dense cluster in the Netherlands known as the core. There are a total of 52 LOFAR stations — 24 core stations, 14 remote stations (also in the Netherlands), and 14 international stations (spread across Europe). The planned construction of an additional international station in Italy will increase this to a total of 53 LOFAR stations. The detailed differences between the station types are described in [van Haarlem et al. \(2013\)](#), one key difference being that international stations have twice the collecting

### 3.2 The REALtime Transient Acquisition Backend (REALTA)

area of a Dutch core or remote station. LOFAR operates in two modes: international mode, also known as International LOFAR Telescope (ILT) mode, and local, or stand-alone, mode. In ILT mode, data from all the LOFAR stations in the network are sent via fibre optics to the COBALT2.0 correlator (an upgrade to COBALT1.0, Broekema et al., 2018) in Groningen, in the Netherlands. In local mode, each international station is operated by the host institute or consortium. *De novo*, international stations do not have dedicated processing backends. Without such an addition the raw data from an international station could not be recorded or analysed.



**Figure 3.1:** Aerial photograph of the Irish Low Frequency Array station IE613 (I-LOFAR) at Birr Castle, County Offaly. Data from the LBAs and HBAs are transferred to the ILT Cabinet (centre right) via coaxial cables where they are amplified, filtered and digitised. In international mode, data are transported to Groningen in the Netherlands at  $\sim 3.2$  Gbps. In local mode, data are processed using REALTA in the I-LOFAR Control Room (bottom left). Image credit: Alison Delaney (Birr Castle).

Construction of the Irish LOFAR station (I-LOFAR) was completed in July 2017 on the demesne of Birr Castle, County Offaly, in the Irish Midlands. An international LOFAR station such as I-LOFAR consists of 96 dual-polarisation dipole antennas known as Low Band Antennas (LBAs) which record radio frequencies of 10 MHz to 90 MHz and 96 High Band Antenna (HBA) tiles which each contain 16 bow-tie anten-

### 3. INSTRUMENTATION

---

nas connected to an analogue summator and record in the frequency range 110 MHz to 250 MHz (see [van Haarlem et al., 2013](#), for a full description of LOFAR antennas). Data recorded by the antennas are then channelised into 512 subbands of 195.3125 kHz (156.25 kHz) frequency resolution at 5.12  $\mu$ s (6.4  $\mu$ s) temporal resolution depending on the clock rate used to sample data, either 200 MHz or 160 MHz ([van Haarlem et al., 2013](#)). The signal from each antenna is then digitally beamformed (BF) to a direction on the sky to create beamlets. A beamlet is a specific location on the sky observed at a specific subband. An international LOFAR station can record and process data in either 8 bits or 16 bits, corresponding to a maximum of 488 or 244 beamlets respectively. The term to describe how many bits are used during an observation is the bitmode. It is also possible to record and process at 4 bits. Beamlets are recorded at 3.2 Gbps. When I-LOFAR is in local mode, the BF data is sent along a fibre connection to a local control room. Fig. 3.1 shows an aerial photograph of I-LOFAR.

The total available bandwidth for I-LOFAR (and other international LOFAR stations) observations is determined by the bitmode used. This corresponds to a bandwidth of  $\sim 47$  (95, 190) MHz for 16 (8, 4) bit data. However, it is not necessary that the frequencies of each beamlet be sequential, which allows a wider range of frequencies to be achieved. This is utilised in ‘mode 357’, developed at the Kilpisjärvi Atmospheric Imaging Receiver Array (KAIRA; [McKay-Bukowski et al., 2015](#)). In mode 357, beamlets are formed such that 200 beamlets from 10 MHz to 90 MHz, 200 beamlets from 110 MHz to 190 MHz and 88 beamlets from 210 MHz to 240 MHz are recorded. In order to achieve this recording scheme, the number of antennas used for each frequency range is reduced. This leads to a lower sensitivity in mode 357. Mode 357 is particularly useful for observations of solar radio bursts, which typically occur across the entire LOFAR spectrum.

I-LOFAR produces a number of one second temporal resolution statistics files which are stored locally on the station’s Local Control Unit (LCU). These are sub-band

### 3.2 The REALtime Transient Acquisition Backend (REALTA)

---

statistics (SSTs), which give the power spectrum for each antenna, beamlet statistics (BSTs), which give the power in each beamlet formed by the LOFAR station, and crosslet statistics (XSTs), the correlation coefficients between each antenna. These low-resolution data can be employed for system monitoring but are also sufficient for some astrophysical applications, for example, the XST data can be used to create snapshot all-sky images, and BST data have been used to study solar radio bursts (Maguire et al., 2020). The desire to use the full capabilities of the station, by accessing the full resolution is the motivation to develop a computational backend for the capture, processing, and storage, of stand-alone BF data.

The REAL-time Transient Acquisition backend (REALTA; from the Irish word for star, *réalta*) is a seven node computer cluster designed to record and analyse the raw BF data from international LOFAR stations in real-time, implemented at I-LOFAR. It takes inspiration from the ARTEMIS backend at the LOFAR-UK station in Chilbolton (Karastergiou et al., 2015; Serylak et al., 2012), although it significantly improves upon its hardware composition, using modern components with greater computational power. The REALTA hardware is available commercially, and as such REALTA can be implemented at any international LOFAR station and is ideal as a generic computing backend for LOFAR local mode observations.

Telescope backends at other international LOFAR stations have been used to search for fast radio bursts (FRBs) and studying pulsars using LOFAR-UK (for example, Karastergiou et al., 2015), the French LOFAR station at Nançay (for example, Bondonneau et al., 2017; Rajwade et al., 2016), and its extension, NenuFAR (for example, Bondonneau et al., 2020), the German stations (e.g Donner et al., 2019; Porayko et al., 2019; Tiburzi et al., 2019), and the combination of a number of international stations (for example, Hermsen et al., 2018; Mereghetti et al., 2016; Michilli et al., 2018). Here we showcase similar success in these and various other observations using I-LOFAR and REALTA.

### 3. INSTRUMENTATION

---

The hardware for REALTA is further described in § 3.2.2 along with the networking configuration for the I-LOFAR control room while § 3.2.3 describes the data capture and processing software used by REALTA. In § 3.2.4, some first scientific results from REALTA are highlighted. These include observations of pulsars, solar radio bursts, FRBs, Jovian radio emission, and the search for extraterrestrial intelligence (SETI).

#### 3.2.2 REALTA

In this section, we describe the local network configuration necessary to capture raw User Datagram Protocol (UDP; [Postel, 1980](#)) packets from I-LOFAR and the individual hardware components that make up REALTA. Data is transferred from the station through the UDP protocol using LOFAR CEntral Processing (CEP) packets. Each packet is 7824 bytes long and consists of a 16 bit header followed by 16 time slices for each beamlet. The full specification for CEP packets is described in both [Lubberhuizen & Kooistra \(2009\)](#) and [Virtanen \(2018\)](#). CEP packets are sent via fibre optics to CEP or REALTA over four data ‘lanes’. Each lane only holds one quarter of the maximum number of beamlets for an observation. The network to facilitate capturing these packets is shown as a schematic block diagram in Fig. 3.2, while Table 3.1 gives a detailed description of the specifications for each of the REALTA nodes.

##### 3.2.2.1 Local networking

The control room for I-LOFAR is located at the Rosse Observatory on the grounds of Birr Castle and  $\sim 100$  m from I-LOFAR (Fig. 3.1). In order to record data from I-LOFAR while it is in local mode, a high-speed 10 Gbps network was set up between the ILT container that houses the I-LOFAR Remote Station Processing (RSP) boards and the control room.

In a typical ILT observation, data output from each RSP board is sent to a Foundry

### 3.2 The REALtime Transient Acquisition Backend (REALTA)

LS648 10 Gbps network access switch (S2) in the container. From here it is sent to a Foundry LS624 switch (S1) before finally being sent over a 10 Gbps fibre connection to the COBALT cluster in Groningen for correlation and or beamforming with data from other LOFAR stations.

The aim of I-LOFAR’s network configuration is to record RSP data to REALTA in the I-LOFAR control room. This is achieved by a fibre link between the I-LOFAR control room and S1. RSP data are sent along a Virtual Local Area Network (VLAN), on a 10 Gbps fibre link to the control room. Data reaches a fibre optic termination panel in the I-LOFAR control room and is sent to a 10 Gbps Dell EMC S4128F-ON optical switch. A fibre link between this switch and the REALTA compute nodes allows data to be recorded. All REALTA compute nodes are connected via Infiniband (an alternative to Ethernet and fibre). On REALTA this acts at a maximum of 10 Gbps to allow for transfer of data between nodes and Network File System (NFS) mounting.

As well as this, a future link to a HEAnet (Ireland’s national education and research network) cloud service for data transfer to the research institutions of the I-LOFAR consortium has been approved by ASTRON. This will allow access along existing 10 Gbps fibre infrastructure to S1 and then over another fibre to the control room along a VLAN. Another fibre is in place to eventually send RSP and Transient Buffer Board (TBB) data directly from S2 to the control room using two additional VLANs. Data transfer from REALTA to research institutes is currently facilitated by a direct 1 Gbps between the Dublin Institute of Advanced Studies (DIAS) and S1 via HEAnet on a VLAN.

#### **3.2.2.2 Hardware description**

REALTA is ultimately designed to perform real-time analysis of radio data generated by the I-LOFAR international station. In its current form, it uses four Dell Poweredge R740XD compute nodes named UCC1, UCC2, UCC3, and UCC4. Each compute

### 3. INSTRUMENTATION

---

node contains two Intel Xeon® Gold 6130 central processing units (CPUs) and an NVIDIA Tesla V100 16GB graphics processing unit (GPU). Each CPU has 16 cores, with two threads per core giving a total of 64 threads per node. A total of 210 TB of storage is distributed across the compute nodes with a further 128 TB available on a dedicated storage server, NUIG1. Storage on REALTA is set up as a Redundant Array of Inexpensive Disks (RAID). Most disks ( $\sim$  263 TB) are in RAID 5 for data archival, while a number of scratch disks ( $\sim$  75 TB) are set up in RAID 0 for recording and processing raw data. In addition to this, a compute node for dedicated SETI research was provided by the Breakthrough Prize Foundation in collaboration with the Breakthrough Listen (BL) team at the Berkeley SETI Research Centre. The BL compute node is a SuperMicro 6049P-E1CR24H node with two, 16 core (8 threads) Intel Xeon® Silver 4110 CPUs, an NVIDIA RTX 2080Ti GPU, and 144 TB of storage. The BL Headnode is a SuperMicro 1029U-TRTP2 node intended to control REALTA during SETI observations. When being operated from the BL Headnode, all of the REALTA compute nodes will receive an identical operating system (OS) image and process in parallel across all five compute nodes. Each of the REALTA nodes connect to the 10 Gbps Dell EMC S4128F-ON optical switch via fibre optic cable as well as a 1 Gbps Ethernet switch for normal networking (using default VLAN 1). There are two redundant keyboard-video-mouse (KVM) servers and a KVM switch for remote access to both switches and all machines, and three uninterruptible power supplies (UPS) to mitigate the effects of a sudden power outage on both servers and critical access paths. Fail-safe cold-aisle air-conditioning will handle heat created by this unsupervised cluster.

REALTA is located in the control room which is  $\sim$  100 m from the I-LOFAR HBAs and  $\sim$  150 m from the LBAs. As REALTA was being set up and tested, the RFI from the system was monitored using all-sky observations and sub-band statistics observations. It was found that REALTA did not produce any significant RFI.

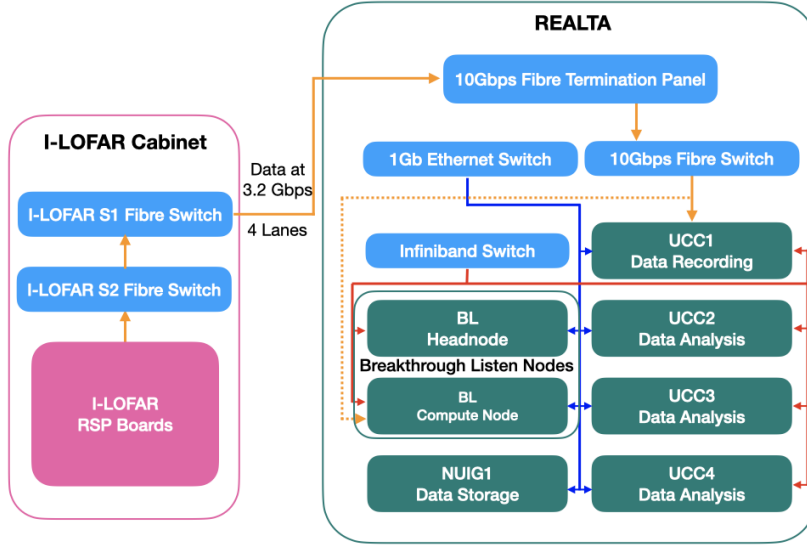


**Figure 3.2:** Block diagram for REALTA and I-LOFAR. Data recorded at the Remote Station Processing (RSP) boards are sent to the S1 fibre switch in the I-LOFAR container. Here the data are split into four ‘lanes’ where each lane contains the data from a maximum of one quarter of the beamlets from the observation. The four lanes of data are then sent over a fibre connection to the I-LOFAR control room where it is recorded by REALTA. Orange arrows indicate the data path along fibre connections. Blue arrows are 1 Gbps Ethernet links and red arrows show infiniband connectivity. The dotted orange line is a fibre link to the BL compute node currently under development.

Table 3.1 lists the technical specifications for each of the nodes in REALTA. In its configuration at the time of writing, REALTA acts as a number of independent nodes (UCC1-4, NUIG1, BL headnode, and BL Compute node). Data is recorded solely to the UCC1 compute node while the remaining nodes perform pre-processing and data analysis after data has finished recording.

### 3.2.3 Software and pipelines

In REALTA’s current state, UDP packets are recorded directly to disk before being converted into usable science products, such as Stokes parameters with variable levels of time integration, after the observation has completed. Future work will implement the current software pipelines to work directly on incoming data, which will allow for real-time analysis of the low frequency sky. Currently, a combination of local

### 3. INSTRUMENTATION

---

	Storage Node (NUIG1)	Compute Nodes ( $\times 4$ UCC1-4 )
Machine Model	Dell Poweredge R730XD	Dell Poweredge R740XD
CPU Model	Intel Xeon® E5-2640 V4 ( $\times 2$ )	Intel Xeon® Gold 6130 ( $\times 2$ )
CPU Clock Speed	2.40GHz	2.10GHz
CPU Cores (Threads)	20 (40)	32 (64)
RAM	256GB	256GB
Storage	128TB	210TB (total)
GPU	N/A	16GB NVIDIA Tesla V100

	BL Headnode	BL Compute Node
Machine Model	SuperMicro 1029U-TRTP2	SuperMicro 6049P-E1CR24H
CPU Model	Intel Xeon® Silver 4110 ( $\times 2$ )	Intel Xeon® Silver 4110 ( $\times 2$ )
CPU Clock Speed	2.10GHz	2.10GHz
CPU Cores (Threads)	16 (32)	16 (32)
RAM	93GB	96GB
Storage	N/A	144TB
GPU	N/A	11GB NVIDIA RTX 2080Ti

**Table 3.1:** Table of hardware specifications for REALTA. Note that the specifications are given for individual UCC 1-4 compute nodes, except for storage which is the total amount dedicated to archival of data distributed across all four.

and community developed software is used in the main data recording and reduction pipeline. The primary recording and processing of the pipeline are described below.

#### 3.2.3.1 Recording data

The station RSPs generate a stream of packets across four data lanes, which is recorded on our compute nodes using software developed by Olaf Wucknitz at the Max Planck Institute for Radio Astronomy. The recording software, `dump_udp_ow`, listens to each port for incoming CEP packets, discards the UDP metadata related to the protocol, and writes the remainder of the packets to disk.

In order to reduce the storage requirements to record the CEP packets, the software can compress the data while it is being captured. This is accomplished by applying the `zstandard` compression algorithm<sup>1</sup> to the output data stream. This procedure requires additional CPU processing but offers a compression fraction in the range of 40-60%, depending on the observing mode and noise of an observation.

#### 3.2.3.2 Pre-processing data

Once the data has been recorded to disk, observers use `udpPacketManager`<sup>2</sup> ([McKenna, 2020](#)), a C library developed to convert the raw CEP packets, either compressed or uncompressed, to usable scientific data products. It implements checks to correct for issues that may have occurred during the recording process, such as padding when packets are missed, performs a polarimetric correction on the voltages using `dreamBeam`<sup>3</sup>, and generates scientific data products for further processing and analysis.

The `udpPacketManager` library is extremely versatile and allows for an observer to chose a number of processing strategies. These include individual polarisation analysis, forming Stokes parameters, ordering data by either time or frequency or formatting

---

<sup>1</sup><https://github.com/facebook/zstd>

<sup>2</sup><https://github.com/David-McKenna/udpPacketManager>

<sup>3</sup><https://github.com/2baOrNot2ba/dreamBeam/>

### 3. INSTRUMENTATION

---

data to be used with other software for further analysis. The most common processing strategy is to construct Stokes I and V from the voltages, then output the results to disk in a binary file format that follows the **SIGPROC** Filterbank standard ([Lorimer, 2011](#)). Future work will include determining best practises for removal of RFI from filterbank formatted files.

#### 3.2.3.3 Pulsar and single pulse processing

All pulse-like observations undergo an additional processing step, whereby data are both channelised by a factor of eight (reducing the bandwidth of a given observing subband to 24.41 kHz) and coherent dedispersion is applied to the voltages. Coherent dedispersion is the process by which an input signal is convolved with the inverse transfer function of the inter-stellar medium in order to remove the signature of dispersion delay due to free elections along the line of sight ([Hankins & Rajkowsky, 1987](#)). This process is especially important at frequencies observed by LOFAR as these delays scale with the inverse square of the observing frequency. This process is performed on the GPUs in REALTA using a modified version of **CDMT** ([Bassa et al., 2017](#)), which accepts input voltages from **udpPacketManager** rather than h5 files generated from the LOFAR COBALT system. In order to avoid distortions caused by Fast Fourier Transform (FFT) operations on zero-padded data, CDMT was further modified to overlap the input voltages between processing iterations.

Pulsar data is further reduced using a combination of **digifil** and **DSPSR** ([van Straten & Bailes, 2011](#)) to generate folded profiles which are then analysed using **PSRCHIVE** ([Hotan et al., 2004](#)). The filterbanks are also often folded using **PRESTO** ([Ransom, 2001](#)) to determine optimal dispersion measures for folding observations. RFI flagging is performed in two steps. Firstly, all data below 106 MHz and above 194 MHz is automatically flagged to remove contributions from local FM radio transmission and to minimise noise contributions due to the loss in sensitivity near the edge

of the telescope’s polyphase filter. Secondly, the spectral kurtosis method is performed by `DSPSR` during the folding step to remove transient RFI sources.

Single-pulse sources, such as intermittent rotating radio transients (RRATs; [McLaughlin et al., 2006](#)) and fast radio bursts (FRBs; [Lorimer et al., 2007](#); [Thornton et al., 2013](#)) are searched for using `Heimdall`<sup>1</sup> to generate pulse candidates across a wide dispersion measure range. A typical search is performed between  $5 \text{ pc cm}^{-3}$  and  $500 \text{ pc cm}^{-3}$  across all pulsar and single-source observations. These are then filtered, discarding any below the  $7.5 \sigma$  level to reduce the number of spurious candidates due to system noise or alignment of RFI between frequency channels. The remaining candidates are then plotted and visually inspected to discard those that are due to RFI, ionospheric scintillation or other phenomena that may cause spurious signals.

#### 3.2.3.4 SETI data processing

For SETI, the goal is to achieve a very high spectral resolution of the order of a few hertz to look for narrow-band Doppler drifting signals. Such signals are prime candidates for deliberately transmitted beacons by Extra-Terrestrial Intelligence (ETI; [Tarter, 2001](#)). Baseband voltages are first recorded as described in § 3.2.3.1 directly on the BL compute node. The `udpPacketManager` library is then used to convert these data to Green Bank Ultimate Pulsar Processing Instrument<sup>2</sup> (GUPPI) formatted baseband data products for further processing. The BL team has developed a suite of software to work with the GUPPI formatted baseband voltages ([Lebofsky et al., 2019](#)) and the preliminary result from this software is discussed in § 3.2.4.

---

<sup>1</sup><https://sourceforge.net/projects/heimdall-astro/>

<sup>2</sup><https://safe.nrao.edu/wiki/bin/view/CICADA/GUPPiUsersGuide>

### 3. INSTRUMENTATION

---

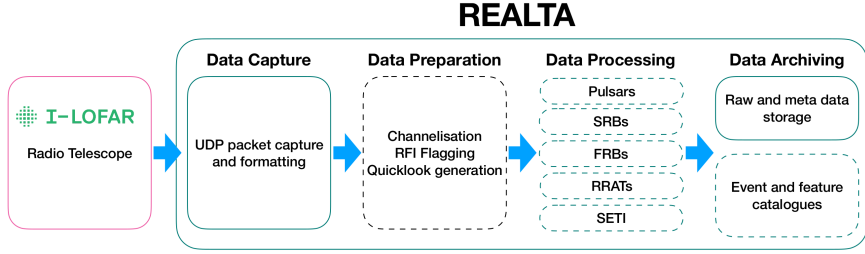


**Figure 3.3:** System diagram for REALTA, including future data preparation, processing, and archiving capabilities. Solid lines indicate existing features, while dashed lines denote stages under development. REALTA is currently capable of capturing data from the I-LOFAR radio telescope and archiving it in near real-time. We are in the process of developing a variety of data processing pipelines that will flag RFI, identify and characterise SRBs, pulsars, RRATs, FRBs, and SETI signals. Machine learning methods are being explored for a number of these tasks.

#### 3.2.3.5 Future development and real-time analysis

The current and planned data path through REALTA, from the time it is recorded at I-LOFAR to when it is written to disk by REALTA is shown as a block diagram in Fig. 3.3. UDP packets containing the data are captured and recorded directly to disk in real-time (§3.2.3.1). The data are then formatted and metadata updated (§3.2.3.2) so that they are compatible with existing pulsar and SETI software (§3.2.3.3, 3.2.3.4).

In the future, the capture and formatting of data will occur simultaneously in real-time. Further channelisation of the raw data in the data capture stage will be implemented in order to increase the spectral resolution of observations and help in flagging Radio Frequency Interference (RFI) in the data. This, along with the generation of quick-look plots, will form the data preparation stage. The data processing software described below will also be developed to allow for real-time processing of solar, pulsar, FRB, RRAT, SETI, and other data. Finally, the data archive will be expanded to include a catalogue of transient events observed and a summary of their features.

### 3.2 The REALtime Transient Acquisition Backend (REALTA)

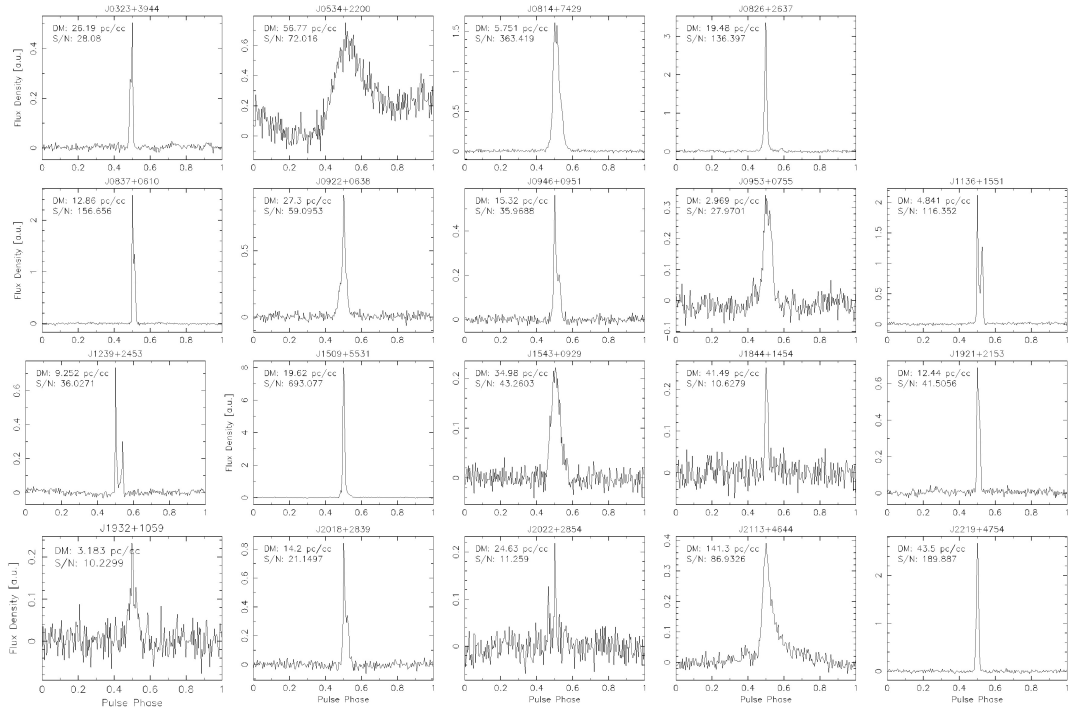


**Figure 3.4:** Sample of 19 pulsars observed with I-LOFAR and REALTA. Each of these observations is 6 minutes in duration and were taken on 4–5 March 2020 using the HBA antennas (110 MHz to 190 MHz). The data were processed using the method described in §3.2.3.3 and plotted using PSRCHIVE. The x-axis in each plot is the pulse phase in radians, while the y-axis is flux density in arbitrary units.

#### 3.2.4 First results

Since REALTA’s installation in July 2018, more than 130 unique targets have been observed. These science use cases range from the Sun, to planetary bodies, to pulsars. This allows for I-LOFAR to be used in the pursuit of a number of science goals. These include: analysing the wide gamut of low-frequency transient phase space (Keane, 2018), characterising pulsars and the characteristics of binary systems (Manchester, 2017), and observing solar activity and space weather (Maguire et al., 2020). REALTA has also enabled collaborations with other LOFAR station operators, most notably an ongoing very long baseline interferometry (VLBI) campaign performed with stations located in Germany, France, and Sweden (in a continuation of Wucknitz, 2019).

The REALTA use cases are complementary to the Key Science Projects of the ILT

### 3. INSTRUMENTATION

---

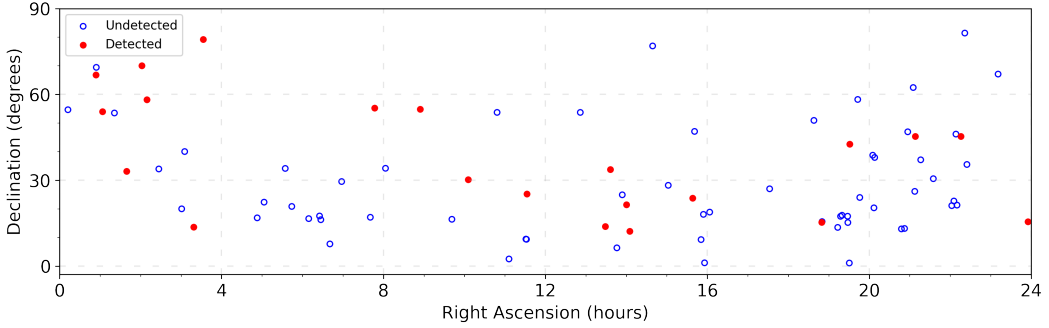


**Figure 3.5:** Overview of the sky positions of the RRATs observed during the census discussed in §3.2.4.2 as of May 2021. Filled red dots indicate sources that have been observed and detected with either single pulses or periodic emission while blue circles indicate sources that were observed but not detected in I-LOFAR data.

(KSP; see [van Haarlem et al., 2013](#)). For example, a single international station is well suited to the study of bright transient sources such as pulsars, rotating radio transients, fast radio bursts, solar radio bursts, Jovian radio emission, and SETI signals, where flexible scheduling can be an advantage (for example, [Maguire et al., 2020](#); [Morosan et al., 2019b](#)). The flexible scheduling of international stations in local mode allows for projects that require a large amount of observing time or regular observations of the same object. International station teams can also use the station to develop and test novel observing campaigns and hardware and software systems (for example, [Scully et al., 2021](#)). First results from the aforementioned science use cases are described below.

#### 3.2.4.1 Pulsars

International LOFAR stations are ideal instruments to observe radio pulsars, particularly at frequencies between 100 MHz and 200 MHz ([Bilous et al., 2014](#); [Noutsos et al., 2015](#); [Stappers et al., 2011](#)). Further, the large fractional bandwidth of an international LOFAR station can offer new insight to the spectral variability of giant pulses from the Crab Nebula. Many international stations regularly participate in pulsar studies (for example, [Bondonneau et al., 2017](#); [Donner et al., 2019](#); [Hermsen et al.,](#)

### 3.2 The REALtime Transient Acquisition Backend (REALTA)

---

2018; Mereghetti et al., 2016), while pulsar observations with LOFAR core stations (for example, Bilous et al., 2020, 2014) are also common. Recent observations with the Polish international stations include those by Blaszkiewicz et al. (2020).

To date, over 50 different pulsars have been observed with I-LOFAR using REALTA. Fig. 3.4 shows a sample of 19 pulsars which were observed, each for 6 minutes, on the 4th and 5th of March 2020, processed using the methods discussed in §3.2.3.3. In addition, as a result of regular timing campaigns of these sources, a number of targets have been studied in more depth, the Crab Nebula being the prime example.

While the recording and timing of folded profiles of the Crab pulsar are of interest for studying the interior structure of the neutron star via its glitches (Lyne et al., 2015) and variability due to scattering and echo events, it also frequently emits so-called ‘giant pulses’ (Meyers et al., 2017). These giant pulses have fluences that vary from hundreds of Jy ms to tens of thousands of Jy ms. These pulses can be studied to analyse their scintillation, scattering, and brightness distributions.

One such example of these giant pulses can be seen in an observation taken of the Crab pulsar with I-LOFAR on 30 June 2020. The observation was processed using the previously described methodology (§3.2.3.2, §3.2.3.3) on REALTA and a short segment of the observation is shown in Fig. 3.6. The figure is made from Stokes I data, where each channel has a bandwidth of 24 kHz and an underlying time resolution of 40.96  $\mu$ s (though it has been interpolated using a median filter for this plot). There were  $\sim 1300$  giant pulse candidates detected in the 30 minute observation. Using a rate of  $\sim 0.7$  giant pulses per second, we determine there are  $\sim 20$  giant pulses visible in the dynamic spectrum in the left panel of Fig. 3.6. Other structure in the left panel of Fig. 3.6 includes some ionospheric scintillation and RFI. This time segment is mostly of interest due to one rare, extremely bright, giant pulse, which is re-plotted in the right panel of Fig. 3.6 where it has been corrected for dispersion effects. Initial analysis using the radiometer equation indicates a specific fluence of  $\sim 200$  kJy ms

### 3. INSTRUMENTATION

---

across the observed bandwidth. Which may be the brightest pulse ever observed for this pulsar at these frequencies ([Karuppusamy et al., 2012](#); [Meyers et al., 2017](#); [Van Leeuwen et al., 2020](#)).

As of May 2021, over 80 hours of observations of the Crab pulsar have been captured by REALTA. Initial analysis of this data set, focusing on a four hour observation from March of 2020, has been performed and given results that are similar to that of other low-frequency instruments. The giant pulses were found to form a fluence distribution with a power-law fit of  $\alpha = -2.86 \pm 0.07$ , similar to that of other low frequency instruments ([Meyers et al., 2017](#)), but steeper than the results at Jodrell Bank ([Mickaliger et al., 2017](#)). Similarly, an initial investigation of the spectral behaviour of the scattering time scales of the brightest pulses appeared to follow a power law of  $\alpha = -3.7 \pm 0.5$ , in agreement with other instruments ([Driessen et al., 2019](#)). Future work includes planning to integrate a CLEAN-based de-convolution (see [Bhat et al., 2003](#)) of the pulse shapes to better describe the scattering and dispersion measure variations of single pulses over time, the effects of which are entangled ([McKee et al., 2018](#)), especially at lower frequencies.

#### 3.2.4.2 Rotating radio transients

Rotating radio transients (RRATs) are a class of neutron star that were discovered through detecting single, bright pulses rather than periodicity searches. If a sufficient number of pulses are detected within a short observing window, it is possible to determine the underlying period of the neutron star through brute force methods, after which the times of arrival of these pulses can be used to time the sources like any other pulsar ([Keane et al., 2011](#)). While the LOFAR core has blindly detected several RRATs during the LOTAAS survey ([Michilli et al., 2020](#); [Sanidas et al., 2019](#); [Tan et al., 2020](#)), and through targeted follow-up observations of sources detected with the Green Bank Telescope ([Karako-Argaman et al., 2015](#)), there has not been a major

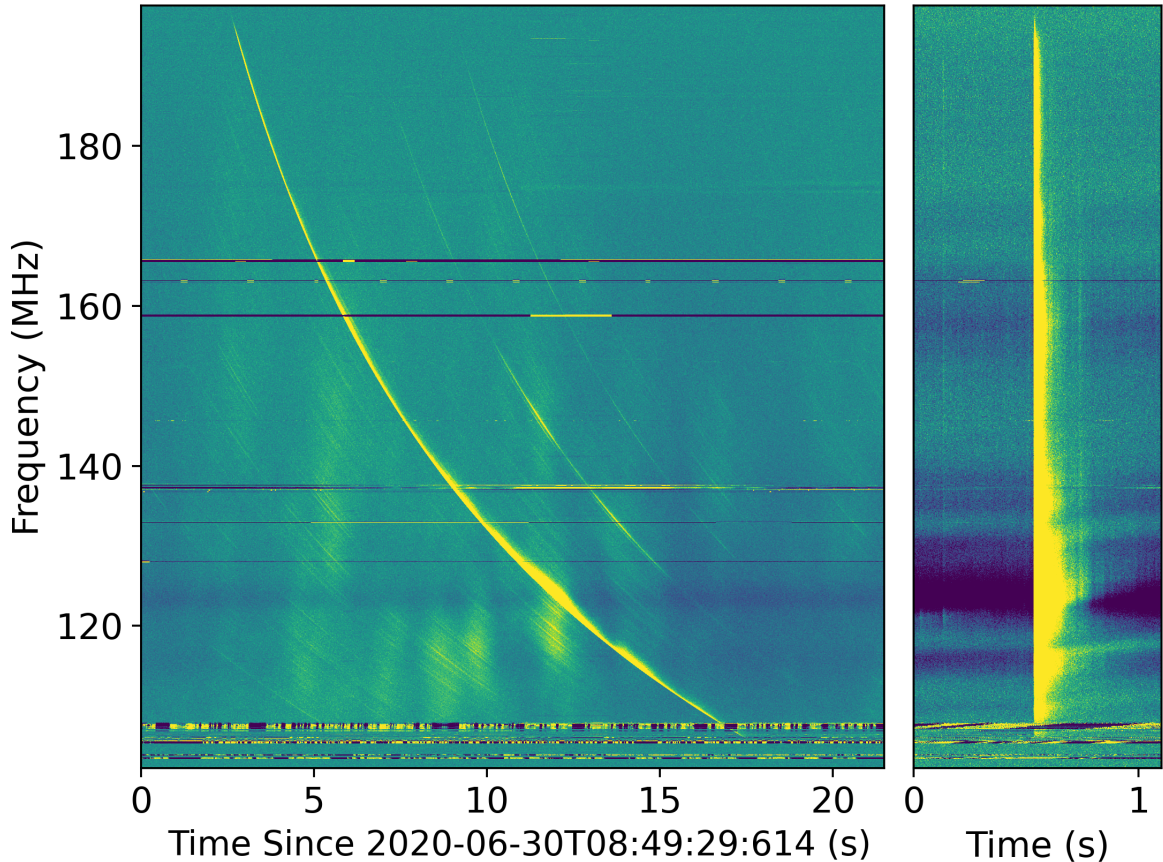


**Figure 3.6:** Observation of the Crab Pulsar performed on 30 June 2020, (left) without incoherent dedispersion and (right) with incoherent dedispersion. The plot on the left contains several giant pulses and both temporal- and spectral-variable ionospheric scintillation. The plot on the right focuses on the brightest pulse in the group, which is the brightest pulse observed from the Crab Pulsar with I-LOFAR to date. Here data were processed to channel bandwidths of 24 kHz, resulting in a sampling rate of  $40.96\mu\text{s}$ . The data were time integrated to a temporal resolution of 1.31 ms prior to plotting.

### 3. INSTRUMENTATION

---

undertaking to time these sources with the LOFAR instruments, using the core or international stations.

However, the full-sky sensitivity and fractional bandwidth of a single international LOFAR station makes it the perfect candidate to perform follow-up observation on some of the brighter RRAT candidates identified by all-sky monitoring instruments such as the Big Scanning Array of Lebedev Physical Institute (BSA LPI) and the Canadian Hydrogen Intensity Mapping Experiment (CHIME; [Amiri et al., 2018](#)). Follow-up observations of these candidates are useful to (a) determine the rotational characteristics of the stars through phase-coherent follow-up timing; and to (b) perform source characterisation from examining stars with broad spectral coverage.

Between July 2020 and May 2021, a 500 hour observing campaign has been undertaken to observe a diverse set of RRATs from the RRatalog<sup>1</sup>, the CHIME-FRB Galactic sources database<sup>2</sup>, and the BSA LPI Transients Catalogue<sup>3</sup>, with a focus on sources that as yet do not have well defined periods. An overview of the sources observed and detected by this census can be seen in Fig. 3.5. This campaign has so far resulted in the discovery of rotation periods for two sources which were previously unknown, periodic detection of a further two sources that have not been previously detected at LOFAR frequencies and the determination of coherent timing solutions for thirteen other sources. These results will be discussed in detail in a future paper (McKenna et al. in prep).

#### 3.2.4.3 Fast radio bursts

Since their discovery in 2007 by [Lorimer et al.](#), fast radio bursts (FRBs) have been of keen interest to radio astronomers across the globe. While blind searches with multiple telescopes have helped push the lower bounds of their emission frequencies down year

---

<sup>1</sup><http://astro.phys.wvu.edu/rratalog/>

<sup>2</sup><https://www.chime-frb.ca/galactic>

<sup>3</sup><https://bsa-analytics.prao.ru/en/transients/rrat/>

### 3.2 The REALtime Transient Acquisition Backend (REALTA)

---

on year, the detection of numerous repeating FRBs by the CHIME-FRB collaboration ([Andersen et al., 2019](#)) has accelerated this process in recent months. Searches for FRBs with LOFAR include those by [Karastergiou et al. \(2015\)](#) and [ter Veen et al. \(2019\)](#), for example.

One particular repeating FRB, FRB 20180916B ('R3') has been found to have a period of  $16.35 \pm 0.15$  days, with an activity window of 5 days ([Amiri et al., 2020](#)), and has been detected with the LOFAR core as of December 2020 ([Pastor-Marazuela et al., 2020](#); [Pleunis et al., 2021](#)). Prior to this, I-LOFAR and REALTA were used as a part of a 70 hour campaign to observe R3 during its activity phase and attempt to see emission at previously unseen frequencies. However, no significant pulse candidates were detected during this campaign. For further results and observations of other FRB sources see [McKenna et al. \(in prep\)](#).

#### 3.2.4.4 Solar radio bursts

Solar radio bursts (SRBs) are some of the brightest phenomena in the radio sky. Five types of SRBs were classified in the 1950s ([Boischot & André, 1957](#); [Wild & McCready, 1950](#); [Wild et al., 1959](#)) and have been studied regularly since (See [Pick & Vilmer, 2008](#), for a comprehensive review). A number of observations of solar radio bursts have been taken either using the LOFAR array as part of the Solar and Space Weather KSP (for example, [Murphy et al., 2021](#); [Zhang et al., 2020](#)) or with an international station during local mode (for example, [Bartosz et al., 2020](#); [Maguire et al., 2020](#); [Morosan et al., 2019b](#)). Most solar radio bursts occur due to the plasma emission process, first described by [Ginzburg & Zhelezniakov \(1958\)](#), and as such can be used as a diagnostic for the plasma density in the solar corona ([Melrose, 1987](#)). Remote sensing of radio emission from the Sun can be used as diagnostics of both large scale energy release from solar flares and CMEs ([Carley et al., 2021](#)) and small-scale energy release, potentially related to coronal heating ([Mondal et al., 2020](#)).

### 3. INSTRUMENTATION

---

On 2 November 2020, I-LOFAR observed a solar radio noise storm in mode 357. The dynamic spectrum of this storm from 12:00 - 14:00 UTC is shown in Fig. 3.7a at 10 ms temporal resolution and 195.3125 kHz spectral resolution. A large number of short duration SRBs are seen across the full HBA band. Fine scale temporal and spectral structure are thought to be indicative of the turbulent nature of the solar corona which could further enhance the diagnostic capability of SRBs (Kolotkov et al., 2018; Reid & Kontar, 2021; Sharykin et al., 2018a).

Some SRBs can exhibit fine scale temporal and spectral features. These include, for example, herringbone bursts which are observed as part of Type II bursts (for example, Carley et al., 2015) or individual striations of a Type IIIb burst (for example, Zhang et al., 2020). A number of short duration radio bursts, which are not part of the five classified types, have also been reported (for example, Ellis, 1969; Ellis & McCulloch, 1967; Melnik et al., 2010a). The high temporal resolution of REALTA observations with I-LOFAR will allow the study of these bursts at some of the highest temporal resolutions to date. Fig. 3.7b shows a zoom-in of the radio noise storm from Fig. 3.7a at 1 ms temporal resolution with an inset showing the sub-second variation of a particular burst. Fig. 3.8 shows an LBA observation from 2 June 2020 of a Type III burst and a U burst, both described by Reid & Ratcliffe (2014), for example, as being generated by electron beams travelling along open and closed magnetic field lines away from the sun respectively. This observation also has a 1 ms temporal resolution. Although a single international LOFAR station can only make spectroscopic observations of Type III bursts and their sub-types, this is still a valuable tool in determining the characteristics of the accelerated electron beam that instigates plasma emission in these bursts (Reid & Kontar, 2018). Further, short duration pulsations in radio bursts can give insight into magnetohydrodynamic oscillations in the solar corona (Carley et al., 2019).

### 3.2 The REALtime Transient Acquisition Backend (REALTA)

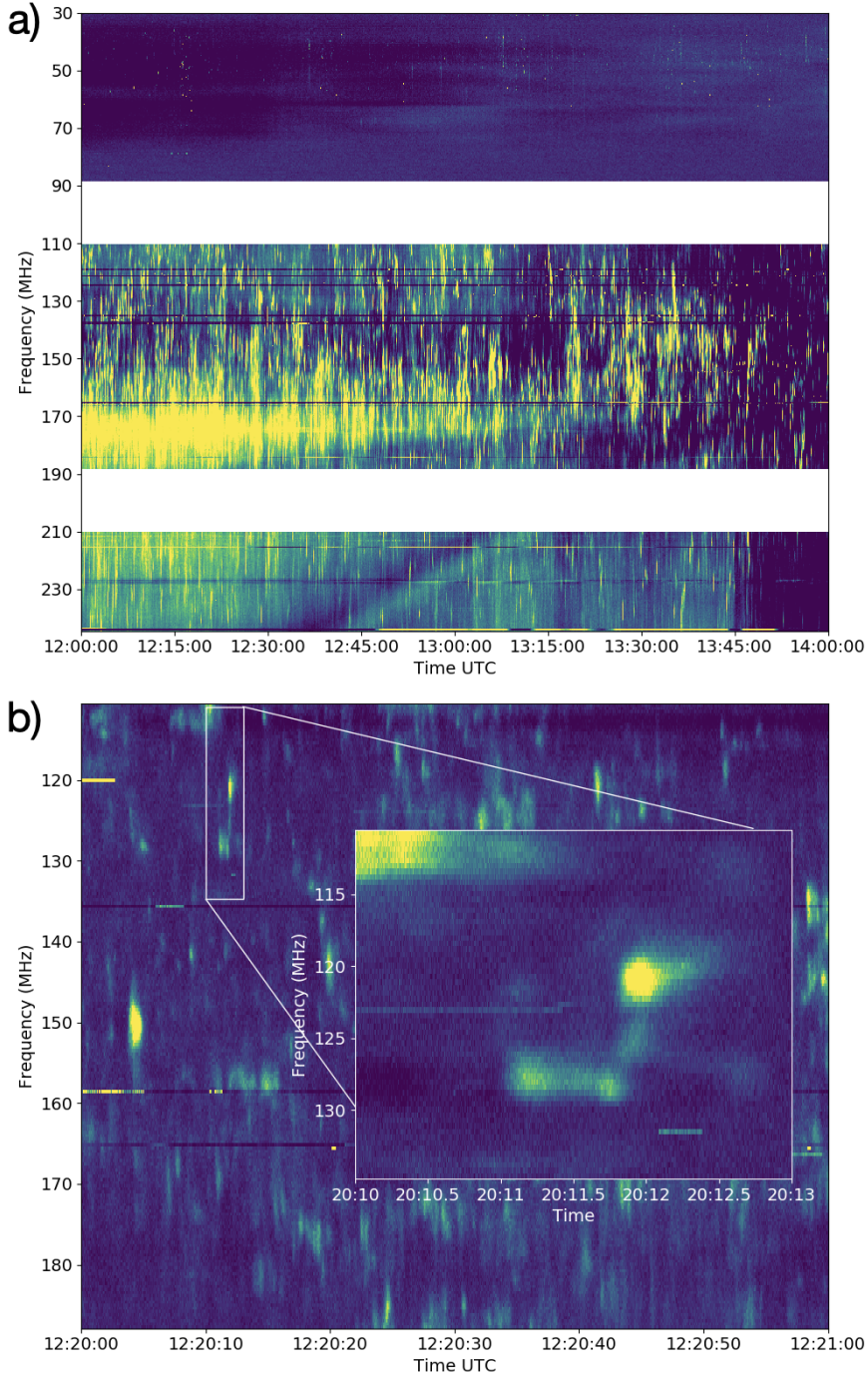


**Figure 3.7:** Solar radio noise storm observed on 2 November 2020. a) In this mode 357 observation, a number of bright bursts can be seen at frequencies greater than 110 MHz (yellow in the dynamic spectrum). Here the data spans 2 hours from 12:00 UTC and has a temporal resolution of 10 ms. b) Zoom-in of panel a) at 1 ms temporal resolution. A number of short duration SRBs are observed. The inset shows the sub-second variation of an individual burst in the noise storm, also at a temporal resolution of 1 ms.

### 3. INSTRUMENTATION

---

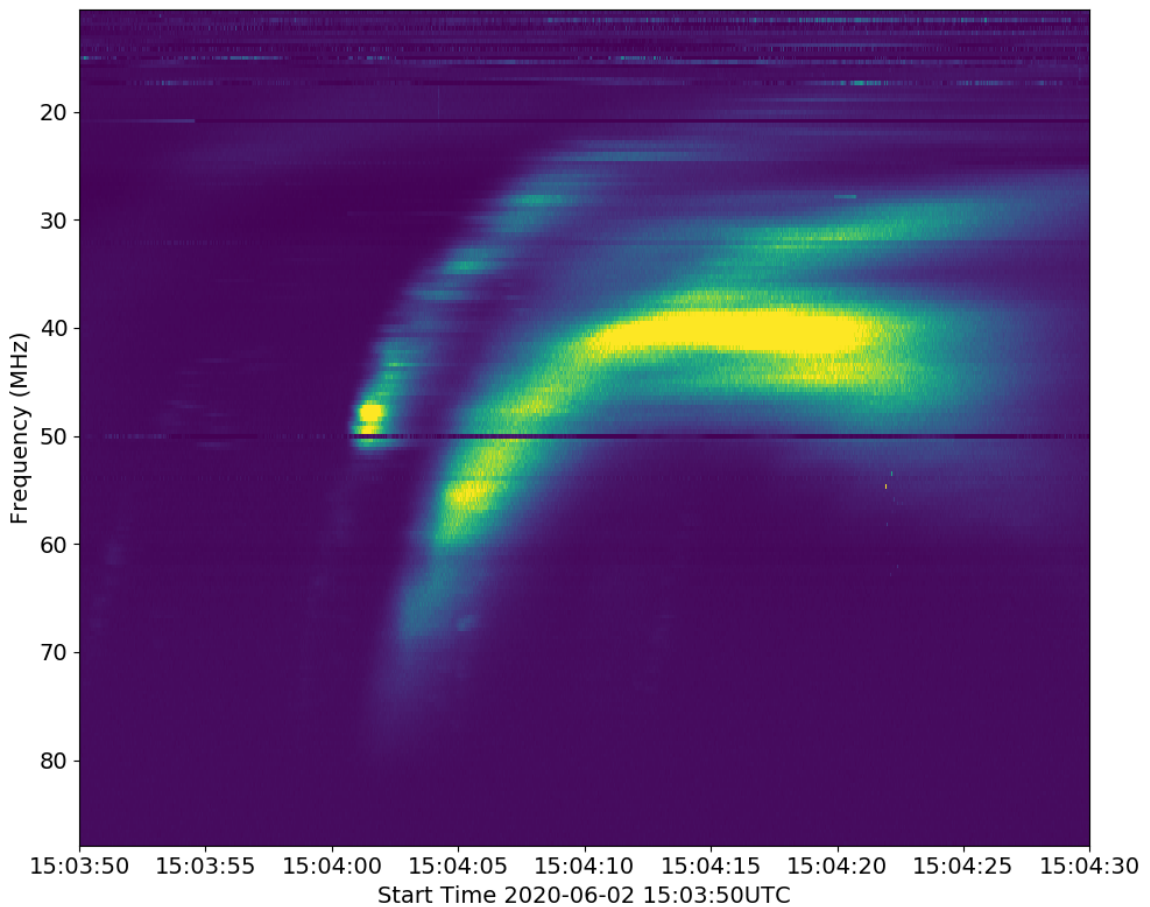


**Figure 3.8:** Two solar radio bursts observed on 2 June 2020. The earlier burst is likely a Type III SRB while the later burst shows the morphology typical of a U burst. The observation has a spectral resolution of  $\sim 195$  kHz and a temporal resolution of 1 ms.

### 3.2 The REALtime Transient Acquisition Backend (REALTA)

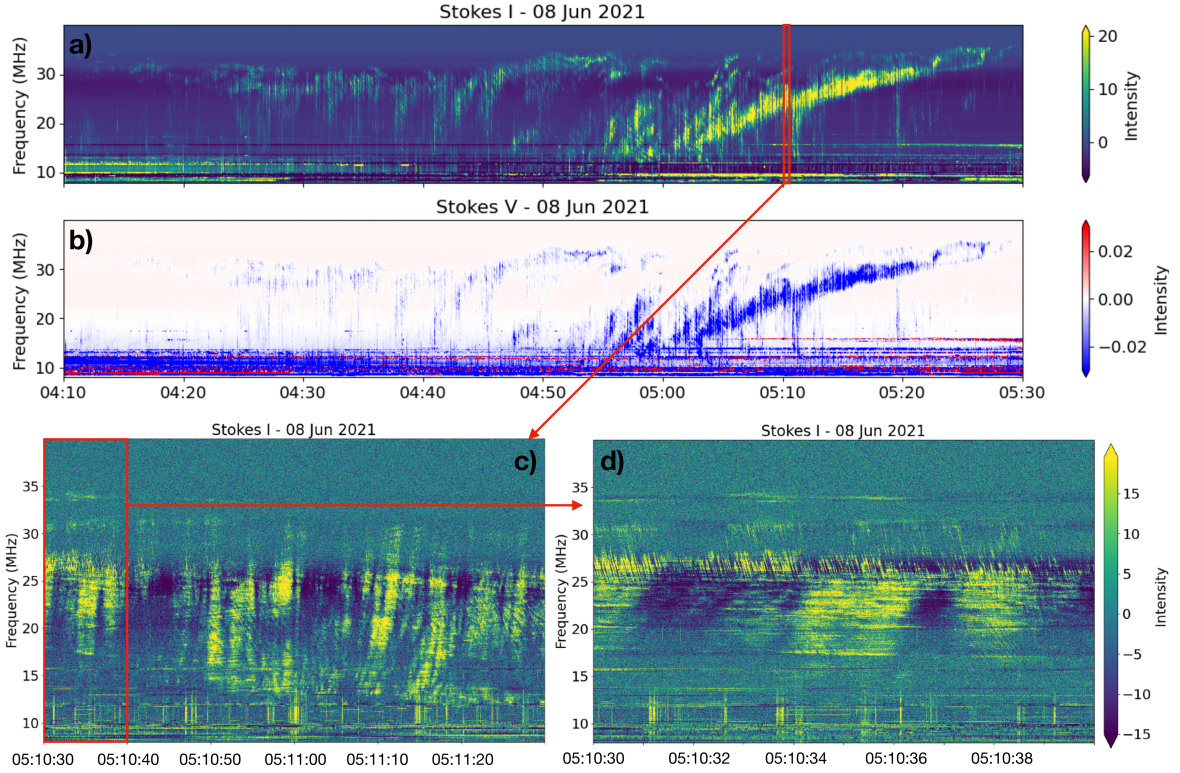


**Figure 3.9:** Observation of a Jovian Decametric emission produced by the Io-Jupiter interaction. Panel (a) shows Stokes I (in dB above background). Panel (b) displays Stokes V (in arbitrary units). The resolution is 84 ms per 12.2 kHz. The emission displays a strong negative value in Stokes V, which means a strong right-hand circular polarization. Panels (c) and (d) show respectively a 60 s and 10 s zoom-in of panel (a) (Stokes I), processed with the highest resolution available for this observation (81.92  $\mu$ s per 12.2 kHz). Millisecond drifting bursts are visible panel (d).

#### 3.2.4.5 Jovian auroral radio emission

Decametric radio emission (DAM), the strongest component of Jovian auroral radiation, was discovered in 1955 by [Burke & Franklin \(1955\)](#), with part of this emission controlled by the Io-Jupiter interaction ([Bigg, 1964](#)). The source of this radio emission is known to be due to the electron cyclotron maser instability (ECMI) in the Jovian magnetosphere, which occurs when a circularly polarised wave resonates with the gyration of electrons with relativistic energies ([Louarn et al., 2017](#); [Treumann, 2006](#); [Wu, 1985](#); [Wu & Lee, 1979](#); [Zarka, 1998](#)). The ECMI amplifies the wave on the extraordinary R-X mode which can escape the source and propagate in free space

### 3. INSTRUMENTATION

---

as a radio wave, at a frequency very close to the local electron cyclotron frequency, which is proportional to the local magnetic field amplitude. Jovian DAM emissions are the only planetary radio emissions visible from the ground, since part of the DAM is emitted at a frequency above the ionospheric cutoff frequency ( $\gtrsim 10$  MHz). BF observations of Jovian DAM using the LOFAR core stations have been used to test the sensitivity of LOFAR to exoplanetary radio emissions (Turner et al., 2019, 2021).

On 8 June 2021, I-LOFAR observed Jovian DAM emission produced by the Io-Jupiter interaction, from 04:10 to 05:30 UTC. The Stokes I and V data from this observation are shown in Fig. 3.9a-b. An arc shape emission with a high intensity is observed between  $\sim 04:55$  and 05:30 (corresponding to the main Io-DAM emission), preceded by emissions with lower intensity starting at  $\sim 04:10$  (corresponding to secondary Io-emissions). Looking at both the shape of the emission and its polarization (strong negative Stokes V value, corresponding to a right-handed circular polarization), we can determine that this emission is an Io-B emission (coming from the north-dawn side of Jupiter, see Marques et al., 2017, for example).

Moreover, we have with I-LOFAR access to very high temporal and frequency resolution, of which an example is shown Fig. 3.9c,d (81.92  $\mu$ s per 12.2 kHz). This will allow us to study the microphysics of the Jovian decametric emissions, for example the millisecond bursts visible Fig. 3.9d with a drifting feature in frequency with time ( $\sim 25\text{-}30$  MHz). These millisecond drifts are thought to be electron bunches propagating along the magnetic field lines and can reveal both the energy of the resonant electrons as well as the potential drops (if present) along these fields lines (Hess et al., 2009, 2007). The high-resolution capability will also enable constraints to be placed on the position and movement of the sources, by interferometric measurements with several LOFAR stations, as well as the characteristics of the emission (for example, thickness and opening of the emission beam). Finally, I-LOFAR, combined with REALTA, is equipped to join the other LOFAR stations in the ground radio observation campaigns

in support of the Jupiter space missions, both current (Juno<sup>1</sup>) and future (JUICE, Europa-clipper).

### 3.2.4.6 SETI

International LOFAR stations such as I-LOFAR have very broad fields of view, particularly at frequencies less than 150 MHz (van Haarlem et al., 2013). This, coupled with the ability to channelise data to bandwidths  $\lesssim 1$  Hz, are favourable characteristics in SETI research. BL is conducting one of the most sensitive, comprehensive, and intensive searches for technosignatures on other worlds across a large fraction of the electromagnetic spectrum (Worden et al., 2017). Targets of the BL program include one million nearby stars, one hundred nearby galaxies, the entire Galactic plane, and exotic astrophysical objects (see Isaacson et al., 2017, for detail). Gajjar et al. (2019) provides the current status of these observing campaigns, as well as listing a number of collaborative observing facilities that are working alongside BL for carrying out these sensitive studies. The BL program is collaborating with two of the international LOFAR stations: I-LOFAR and LOFAR-SE, which is located at Onsala (Sweden), to complement searches towards the above-mentioned BL targets at lower radio frequencies. Details of the dedicated hardware deployed at I-LOFAR is discussed in §3.2.3.4. First-light observations were conducted with these BL nodes on 19 November 2020 towards PSR B1919+21 to validate the BL recording and conversion pipelines. Recently, we also conducted observations of PSR B2217+47 on 21 April 2021 using the BL nodes for further pipeline development. Baseband data in the GUPPI format were converted to two different temporal and spectral resolution total intensity SIGPROC formatted filterbank data products. PSR B2217+47 was clearly detected, by folding high-temporal products. To search for narrowband Doppler drifting signals, SIGPROC

---

<sup>1</sup>Such as the Juno Ground Radio Observation Support <https://maser.lesia.obspm.fr/task-1-data-collections/juno-ground-radio/>

### 3. INSTRUMENTATION

---

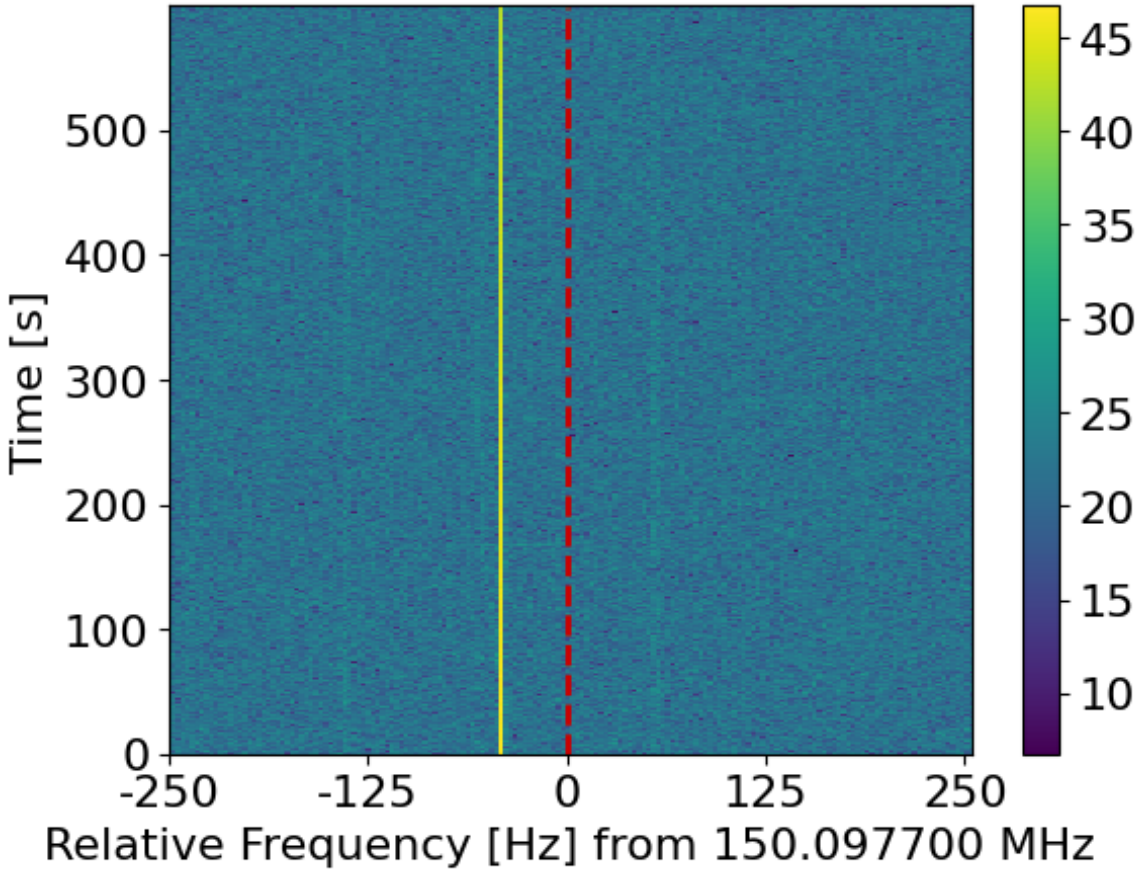


**Figure 3.10:** Narrowband signal detected using REALTA and the `turboSETI` algorithm. Dynamic spectra of an example narrowband signal detected in an observation pointing toward PSR B2217+47 using `turboSETI` with the BL nodes in REALTA. The colour bar shows intensity in arbitrary units while the red dotted line shows a relative frequency of 0 Hz from 150.0977 MHz. The signal does not show any drifting and thus likely has a terrestrial origin.

formatted filterbank files with 3 Hz spectral resolution were used. This made use of the BL narrowband signal search tool, `turboSETI` (Enriquez et al., 2017). Fig. 3.10 shows an example of one of the narrowband signals of terrestrial origin detected using `turboSETI` towards PSR B2217+47. In the future, it is planned to conduct detailed on-target and off-target observations to discriminate such anthropogenic signals from true sky-bound ETI signals.

### 3.2.5 Conclusions and future work

We have described the hardware for REALTA and given an overview of the software used to record and analyse data recorded from I-LOFAR. Several first result observations were showcased, exhibiting the broad range of objects that I-LOFAR and REALTA can observe.

LOFAR 2.0 is a series of hardware and software upgrades to the ILT, which will be implemented in a number of stages over the coming years. An upgrade to an international LOFAR station, such as I-LOFAR, will require new receiver units (RCU2), new station beamformers (Station Digital Processors) based on the Uniboard<sup>2</sup> architecture (Schoonderbeek et al., 2019) and new power, clock and control board for improved station control. The upgrade will greatly improve the instantaneous bandwidth, sensitivity and RFI rejection of an international station.

LOFAR for Space Weather (LOFAR4SW)<sup>1</sup> is a proposed upgrade to LOFAR, currently being designed to enable regular space weather monitoring. If completed, LOFAR4SW would allow near-real-time monitoring of space weather phenomena such as solar flares and coronal mass ejections, interplanetary scintillation and ionospheric disturbances (Carley et al., 2020). This is useful not only to space weather researchers but to the radio astronomy community as a whole as it will broaden our understanding of how space weather can effect the propagation of radio waves in the inner heliosphere and disturbances in the ionosphere and the effect this has on observing astronomical sources. In order to record the data streams from a LOFAR4SW enabled international station in local mode, a backend such as REALTA will be required to capture the data-stream and to process the raw data so that it can be used by space weather researchers and forecasters. The effectiveness of machine learning algorithms to detect solar radio bursts with REALTA is currently being investigated.

---

<sup>1</sup><https://www.lofar4sw.eu>

### 3. INSTRUMENTATION

---

In the future, REALTA will be upgraded to fully include the BL headnode into the system. In order to achieve this, additional VLAN fibre connections will be set up between the UCC compute nodes and the BL headnode and compute nodes. Activating these VLAN fibre connections will allow each machine to record one lane of data and perform real-time channelisation and dedispersion making use of their GPUs. The BL headnode will distribute an identical OS to the UCC and BL compute nodes and control them in parallel. This will allow REALTA to monitor for radio transients such as those important to SETI research. Upgrades to the data preparation and processing stages of the REALTA data flow (Fig. 3.3) will see REALTA operating fully in real-time (see §3.2.3.5).

With future upgrades to ILT hardware coming in the first half of the 2020s (mainly LOFAR2.0; [Edler et al., 2021](#)), international LOFAR stations will require a dedicated high-performance backend to record data rates of  $\sim$ 6.4 Gbps, should they wish to use the full capacity of the instrument in local mode. While some international stations have existing backends, REALTA offers a powerful backend that is well suited to the data rates of LOFAR2.0. Backends like REALTA, due to the use of commercially available hardware, straight-forward network configuration and freely available software, will make it possible for international LOFAR stations to capture and process raw data, and to undertake a wider variety of astronomical observations. As mentioned in §3.2.3.5, in the future it will be possible to process and record raw data in real-time. This will be done by recording data to a ring buffer implemented with the Parkes-Swinburne Recorder Distributed Acquisition and Data Analysis software (PSRDADA; [Jameson & van Straten, 2008](#)) and then reading from the ring buffer into `udpPacketManager`. This will further improve the capabilities of international LOFAR stations during local mode. Finally, cooperation and coordinated observations between international LOFAR stations becomes easier if using the same software and hardware for data capture and post-processing and will be more beneficial than

### 3.2 The REALtime Transient Acquisition Backend (REALTA)

each international station operating individually.

### 3. INSTRUMENTATION

# Measuring Source Sizes in Visibility Space

Low frequency radio wave scattering and refraction can have a dramatic effect on the observed size and position of radio sources in the solar corona. The scattering and refraction is thought to be due to fluctuations of electron density caused by turbulence. Hence, determining the true radio source size can provide information on the turbulence in coronal plasma. However, the lack of high spatial resolution radio interferometric observations at low frequencies such as with the LOw Frequency ARray (LOFAR) have made it difficult to determine the true radio source size and level of radio wave scattering. Here we directly fit the visibilities of a LOFAR observation of a Type IIIb radio burst with an elliptical Gaussian to determine its source size and position. This circumvents the need for imaging of the source followed by deconvolution, which can introduce spurious effects on source size and shape. For a burst at 34.76 MHz, we find a full width at half maximum height (FWHM) along the major and minor axes to be  $18.8' \pm 0.1'$  and  $10.2' \pm 0.1'$  respectively at a plane of sky heliocentric distance of  $1.75 R_{\odot}$ . Our results suggest that the level of density fluctuations in the solar corona is the major cause of the scattering of radio waves, resulting in large source sizes. However, the magnitude of  $\varepsilon$  may be smaller than previously derived in comparison to observations of radio wave scattering in tied-array images.

## 4.1 Introduction

Low frequency radio wave propagation in the solar corona is not fully understood. It is widely accepted that scattering of radio waves off of density inhomogeneities plays a key role in the observed source sizes of radio bursts (Fokker, 1965; Kontar et al., 2019; Riddle, 1974; Steinberg et al., 1971; Stewart, 1972; Thejappa & MacDowall, 2008; Thejappa et al., 2007). However, the exact extent to which observed source sizes

#### 4. MEASURING SOURCE SIZES IN VISIBILITY SPACE

---

are broadened is difficult to measure as it requires an angular resolution to spatially resolve the source as well as an *a priori* knowledge of its original size. Current generation radio interferometers such as the LOw Frequency ARray (LOFAR; ?) have the resolving power to observe this angular size. This angular resolution can be exploited to accurately determine burst size and position, both of which are indicators of the level of radio scattering in the corona, which in turn is related to the level of turbulent density fluctuations. Hence a better understanding of scattering may lead to new insights into the nature of coronal turbulence.

The study of radio wave scattering in the solar corona has its origins in the 60s and 70s. Fokker (1965), Steinberg et al. (1971), Stewart (1972) and Riddle (1974) did seminal work on ray tracing of radio waves in various coronal models. All concluded that sources emitted near the plasma frequency in the solar corona are enlarged due to scattering of radio waves from coronal density fluctuations. While the explanation of coronal scattering for observed source characteristics fell out of favour by the mid 1980s (McLean & Labrum, 1985), it has seen renewed interest in low frequency radio observations in recent years (Gordovskyy et al., 2019; Kontar et al., 2019, 2017; Sharykin et al., 2018b; Thejappa & MacDowall, 2008; Thejappa et al., 2007).

In low frequency imaging, the extent of scattering in the corona can be determined through the analysis of Type III radio bursts, particularly their position and size in images or decay times in dynamic spectra (e.g. Gordovskyy et al., 2019; Kontar et al., 2019; Krupar et al., 2018). Given that these bursts are due to plasma emission from electron beams propagating through coronal plasma (see Reid & Ratcliffe, 2014, for a review), they provide a density diagnostic of such plasma. In particular, a subset of these bursts known as ‘Type IIIb’ provide a diagnostic of scattering in coronal plasma due to density fluctuations from turbulence. For example, Type IIIb bursts often show fine structures or ‘striae’ along the burst envelope (de La Noe, 1975; de La Noe & Boischot, 1972; Ellis, 1969; Ellis & McCulloch, 1967; Melnik et al., 2010b),

which are believed to be caused by density inhomogeneities in the corona ([Takakura & Yousef, 1975](#)). Using a density model, the frequency bandwidth of these striae can be used to infer the vertical extent of the density inhomogeneity in space. A comparison of this spatial extent to observed source size in images can provide the extent to which the radio emission has been scattered (e.g. [Kontar et al., 2017](#)).

Theoretically, the extent of scattering in the corona is related to the root mean squared (r.m.s) fluctuations of electron density  $\varepsilon = \sqrt{\langle \delta n^2 \rangle} / n$ . Many recent works have assumed a value for  $\varepsilon$  to use in simulations in order to recreate the time profile and source size of solar radio bursts (e.g. [Kontar et al., 2019](#); [Krupar et al., 2018](#)). However, few use the observed source size and time profile to determine  $\varepsilon$ . Those that have are limited to determining the value of  $\varepsilon$  in the solar wind at distances  $> 10 R_\odot$ . Techniques such as interplanetary scintillations (e.g. [Bisoi et al., 2014](#)) and crab nebula occultation ([Sasikumar Raja et al., 2016](#)) have also been used to determine  $\varepsilon$  at these distances. The general conclusion of these studies is that  $\varepsilon$  varies slowly with heliocentric distance and has typical values of  $0.001 \lesssim \varepsilon \lesssim 0.02$  in the range of 10 to 45  $R_\odot$ . Despite this, larger values of  $\varepsilon$  have been used in models. For example, [Reid & Kontar \(2010\)](#) use a value of  $\varepsilon \approx 0.1$  to model electron beam transport while [Kontar et al. \(2019\)](#) recently used Monte Carlo simulations of scattering to determine that a value of  $\varepsilon = 0.8$  is necessary in order to account for source sizes of the order of 20', as observed by [Kontar et al. \(2017\)](#). Measured values of  $\varepsilon$ , particularly at heights of  $\sim 2 R_\odot$ , are not common in the literature, with the exception of a recent study by [Krupar et al. \(2020\)](#). By using observations from Parker Solar Probe (PSP, [Fox et al., 2016](#)), [Krupar et al. \(2020\)](#) calculate a value for  $\varepsilon = 0.07$  at a plasma frequency  $f_p = 137$  kHz. They also find that the value of  $\varepsilon$  decreases from 0.22 to 0.09 over a height range of 2.4 to  $14 R_\odot$ .

It is clear that a correct interpretation of radio observations provide a means to investigate the level of scattering and density fluctuation in the corona. Advances in

## 4. MEASURING SOURCE SIZES IN VISIBILITY SPACE

---

radio astronomy over the past 40 years have lead to increased sensitivity, temporal resolution, frequency resolution and resolving power. Modern radio telescopes such as LOFAR, the Murchison Widefield Array (MWA; [Lonsdale et al., 2009](#)) and the upcoming Square Kilometre Array (SKA; [Dewdney et al., 2009](#)) are capable of observing the predicted spatial and time profiles of Type IIIb bursts. That said, previous studies with LOFAR have tended to use tied-array imaging in this regard ([Kontar et al., 2017](#)), which has limited spatial resolution with respect to interferometric imaging.

In this paper we use LOFAR interferometric observations to determine the observed radio source size and position and how this differs from the expected source properties, which can be estimated from spectroscopy. Directly fitting interferometric visibilities provides us with the opportunity to observe low frequency radio sources at a spatial resolution in excess of what has usually been achieved. We compare our results with those of the tied-array observation from [Kontar et al. \(2017\)](#) and discuss the implication this may have on determining the relative level of density fluctuations in the corona. The remainder of this paper is outlined as follows; an observation of a Type IIIb burst is described in Section 4.2, in Section 4.3 we detail a method of directly fitting interferometric visibilities in order to recreate a sky brightness distribution and give results of observed source size. Section 4.3 also includes analysis of a Type IIIb stria. We conclude with a discussion in Section 4.4.

### 4.2 Observation

LOFAR is an interferometric array that spans across Europe observing radio frequencies at 10 - 240 MHz. An interferometric observation of the Sun, utilising 36 stations (24 core and 12 remote), was performed on 17 October 2015 from 08:00 UTC to 14:00 UTC. During this time, a Type III solar radio burst was recorded at 13:21 UTC. A calibrator source, Virgo A, was observed co-temporally in all subbands over the course

of the observation.

Figure 4.1a shows the X-ray flux measured by GOES for the duration of the LOFAR observation. A number of C-class flares can be seen in Figure 4.1a but no significant activity is noticeable at the time of the radio burst, indicated by red vertical lines

A dynamic spectrum of the burst was recorded in the LBA band by remote station RS509 and is shown in Figure 4.1b. The inset shows a number of striations from 34 - 35 MHz and the white cross indicates the time and frequency at which the images described in Section 4.3 are made.

The maximum baseline of the LOFAR observation is 84 km giving sub-arcminute resolution across almost all of the observed frequency range, offering an unprecedented level of spatial resolution.

### 4.3 Data analysis and results

The source sizes and positions of solar radio bursts in LOFAR data have typically been obtained by the “tied-array imaging mode” (Morosan et al., 2014) whereby a number of beams are tessellated across the sun and the response in each beam is interpolated to produce an image (e.g. Kontar et al., 2017; Morosan et al., 2019a; Reid & Kontar, 2017; Zucca et al., 2018). Tied-array imaging has the distinct advantage over interferometric observations in that it retains the  $\sim$ 12 kHz frequency resolution and  $\sim$ 0.01 s temporal resolution from LOFAR beamformed observations but it also contains a significant limitation. Tied-array observations can only be made using the LOFAR core stations as they share a single clock (de Gasperin et al., 2019), which makes it possible to add beamformed data coherently. This means that the maximum baseline from tied-array observations is approximately 2 km corresponding to an angular resolution of  $\sim$ 17' at  $\sim$ 30 MHz. Not only this, but the effect of interpolation between each tied-array beam on the observed source size has not yet been compared

#### 4. MEASURING SOURCE SIZES IN VISIBILITY SPACE

---

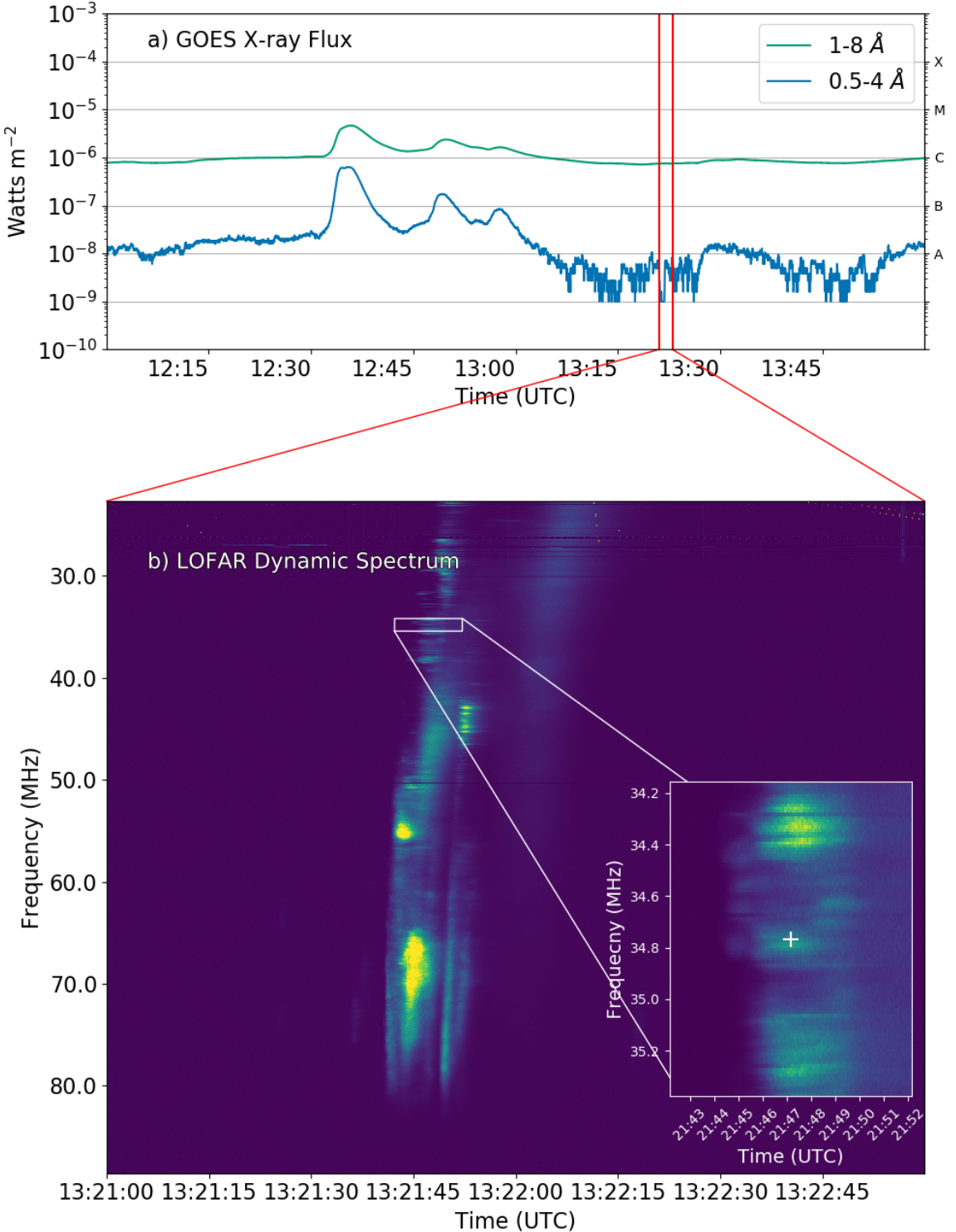


**Figure 4.1:** a) GOES X-ray lightcurves for the duration of the LOFAR solar observation. Minimal activity other than a number of C class flares prior to 13:00 UTC is observed. Red vertical lines indicate the time range of radio analysis. b) Dynamic spectrum of a Type III solar radio burst observed with LOFAR station RS509. We note the striations in frequency which are particularly apparent below 40 MHz. The inset is a zoom of the region in the white box showing striation in the burst. The white cross indicates the time and frequency at which the images described in Section 4.3 are made.

to observations done interferometrically. It is therefore unclear whether previously observed source sizes are in fact due to the underlying source, or an effect of the imaging technique. Solar campaigns with LOFAR are now performed with a new mode which allow for simultaneous interferometric and tied-array observations. A detailed comparison of these modes is currently under study, which should resolve the ambiguity in source sizes determined with tied-array observations (Morosan, D. E. 2020, private communication).

In order to avoid such limitations of the tied-array mode, here we use interferometric observations from the LOFAR core and remote stations, offering a longer baseline of 84 km and hence much better spatial resolution. The LOFAR data from this observation were calibrated using the Default Preprocessing Pipeline (DPPP; [van Diepen et al., 2018](#)) and a co-temporal observation of Virgo A. This corrects for effects such as antenna band-pass, clock drift and propagation effects through the ionosphere ([de Gasperin et al., 2019](#)). We next describe our technique of directly fitting the LOFAR visibilities to estimate radio source size and position.

To produce an image from interferometric observations an inverse Fourier transform is performed on the observed visibilities, usually followed by a deconvolution of the array point spread function (PSF) from the resulting ‘dirty-map’ of the sky-brightness distribution. For such a deconvolution, LOFAR uses an implementation of the multi-scale CLEAN algorithm known as WSClean ([Offringa et al., 2014](#)). In this procedure a weighting may be applied to the visibilities to improve sensitivity to various spatial scales, the most common of which is the Briggs robustness weighting scheme ([Briggs, 1995](#)). Recreating a radio image in this way can introduce artefacts depending on the Briggs robustness used, the number of iterations of the algorithm and a number of other parameters described in more detail in [Cornwell \(2008\)](#); [Högbom \(1974\)](#); [Offringa et al. \(2014\)](#); [Offringa & Smirnov \(2017\)](#) for example. These artefacts include changes to the source shape and size. Therefore, to avoid ambiguity in the source

## 4. MEASURING SOURCE SIZES IN VISIBILITY SPACE

---

size, shape and position due to such imaging algorithms, we directly fit the measured visibilities similar to a method used for X-ray observations using the Reuven Ramaty High Energy Solar Spectroscopic Imager (RHESSI [Hurford et al., 2002; Kontar et al., 2010](#)). We describe our method in the following subsections.

### 4.3.1 Fitting the visibilities

The  $uv$  plane is a Fourier space representation of antenna pair positions. Each point in the  $uv$  plane is sensitive to emission of a particular angular scale. Due to the timescales over which Type III bursts occur, solar observations are limited to a sparse sample of the  $uv$  plane and techniques to increase samples in this plane, such as aperture synthesis, cannot be used. However, the large brightness temperatures of Type III and Type IIIb radio bursts ([Reid & Ratcliffe, 2014](#)) give rise to a high signal to noise ratio which allows a direct fit of a model to the visibilities. In the following we assume that the emitting source is a single elliptical Gaussian. This is based on the dynamic spectrum in Figure 4.1b, showing the Type IIIb burst does not overlap any other bursts and as such is probably the only source in an interferometric image. The assumption leads to the convenient fact that an elliptical Gaussian in real space is observed as another elliptical Gaussian in the  $uv$  plane. The form of this Gaussian is

$$V(u, v) = e^{-2\pi i(ux_0 + vy_0)} \left( \frac{I_0}{2\pi} e^{-\left(\frac{\sigma_x^2(2\pi u')^2}{2} - \frac{\sigma_y^2(2\pi v')^2}{2}\right)} + C \right) \quad (4.1)$$

where  $x_0, y_0$  are the x and y coordinates of the source centre in real space,  $\sigma_x, \sigma_y$  are the standard deviation in the x and y direction and  $C$  is a constant background. Here the visibilities have been rotated to a new coordinate frame with axes  $u'$  and  $v'$  which are parallel and perpendicular to the major and minor axes of the Gaussian source such that  $u' = u \cos \theta - v \sin \theta$ ,  $v' = u \sin \theta + v \cos \theta$ , where  $\theta$  is the angle of the major axis to the x axis, i.e. the position angle of the Gaussian on the  $uv$  plane.

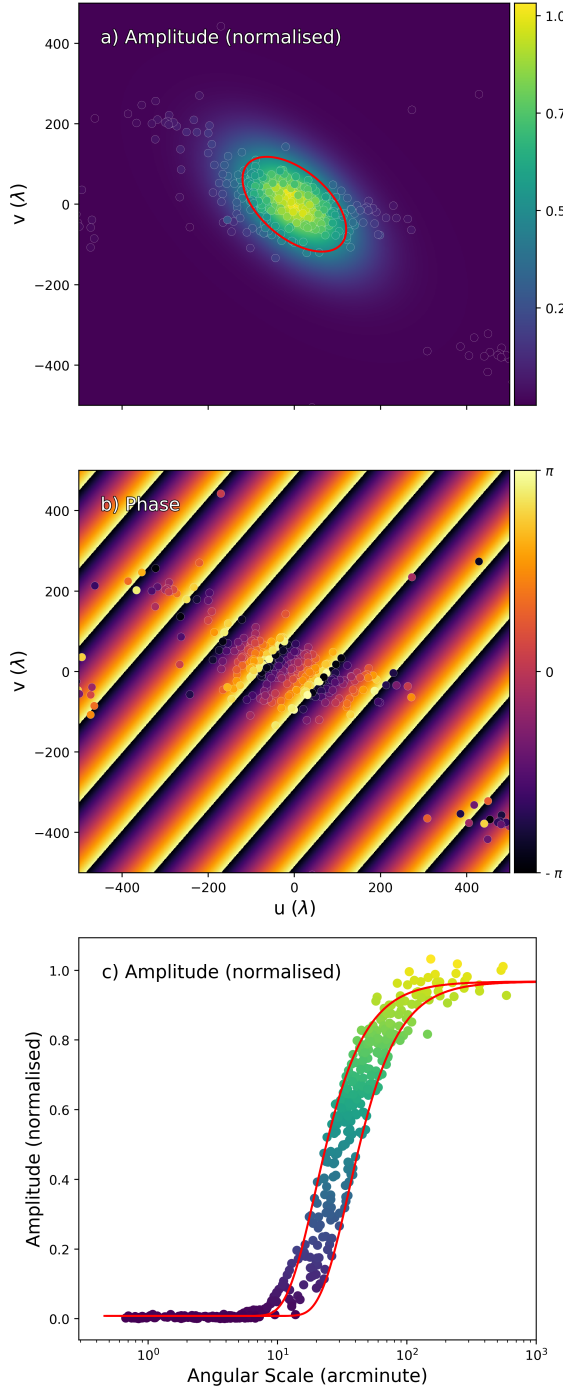
A nonlinear least squares fit is applied to the sample of visibilities in two stages. First, the source size, maximum intensity and angle relative to the x axis are found by fitting the absolute value of the complex visibilities. In order to determine source location, the phase angle of the data is fit. Source location in real space determines fringe separation and orientation in Fourier space. The direct fitting of parameters to  $V(u, v)$  is then used to recreate the sky brightness distribution or image  $I(x, y)$ , which is the inverse Fourier Transform of Equation 4.1.

Figure 4.2 shows the fit of the modelled Gaussian to the complex visibilities. Due to the fact that this fit is done in Fourier space, the amplitude and phase of the data and fit are shown in the  $uv$  plane in Figure 4.2a and 4.2b respectively. Here, the points are the observed visibilities and the background colour map is the fit. In Figure 4.2a a red ellipse indicate the full width at half maximum height (FWHM) of the fitted Gaussian. The fringes in Figure 4.2b show the fit of the source position to the distribution of visibility phases across  $uv$  space. Figure 4.2c shows the increase in the amplitude of recorded visibilities with the angular scale on the sky that causes this increase. The red curves are where data points would lie for a Gaussian in visibility space with the FWHM in the major and minor direction obtained from the fit in Figure 4.2a.

The visibility fit reveals a source with a FWHM in real space of  $18.8' \pm 0.1'$  and  $10.2' \pm 0.1'$ , in the direction of the major and minor axis, respectively. The source is found at a position of  $-1312'', -1064''$  from the solar centre giving a plane of sky distance of  $1.75 R_\odot$ . The parameters from the fit can then be used to recreate a sky-brightness distribution  $I(x, y)$  in real space which is shown as contours over-plotted on a  $171\text{\AA}$  image taken by the Atmospheric Imaging Assembly (AIA; Lemen et al., 2012) in Figure 4.3. We note that despite the theoretical high angular resolution of the long baselines afforded by LOFAR remote stations (84 km), the source size is still large and we see little evidence of angular scales smaller than  $\sim 10'$  in Figure 4.2c. We will discuss this further in Section 4.4.

## 4. MEASURING SOURCE SIZES IN VISIBILITY SPACE

---



**Figure 4.2:** a) Amplitudes of visibilities in the  $uv$  plane for LOFAR observation. Background colour map shows a Gaussian fit. Red ellipse shows the FWHM of the normalised amplitude. b) Visibility phase in the  $uv$  plane. Background colour map shows fitted phase angle. c) Visibility amplitudes received from different angular scales. Red curves indicate the FWHM of the semi-major and semi-minor axes of the fitted Gaussian.

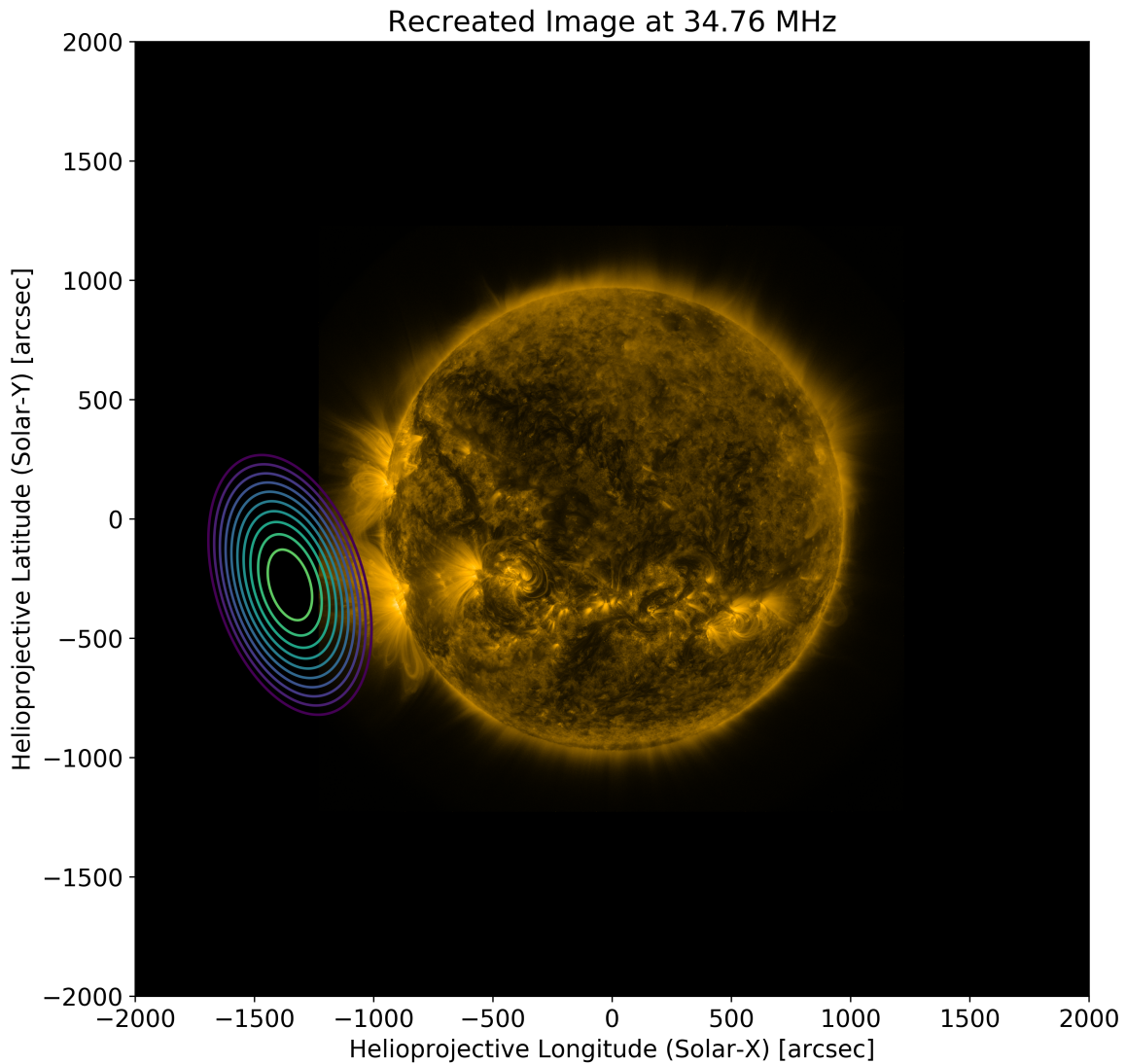


**Figure 4.3:** Recreated sky intensity profile of a Type IIIb radio burst occurring at 13:21:46 on 17 October 2015. The background solar image is an AIA 171Å image at 17 October 2015 13:21:46 UTC.

### 4.3.2 Type IIIb striae

In the above we determined the source size and position using a direct modelling of LOFAR visibility observations. This provides us with an opportunity to compare the observed source size to its actual size, which can be estimated from spectroscopic observations, similar to the method of [Kontar et al. \(2017\)](#).

To estimate the source size from spectroscopic measurements, we relate the FWHM of the frequency of the striation to its vertical extent in the solar corona  $\Delta r \sim 2L$  ( $\Delta f/f$ ) where  $L$  is the characteristic density scale height ([Kontar et al., 2017](#)). A single striation was manually identified at 34.76 MHz from the dynamic spectrum. The time of maximum intensity for the burst was found and a vertical frequency slice was obtained from which  $\Delta f/f$  was calculated. The individual striation, the centre of which is indicated by a white cross in the inset panel of Figure 4.1b, was fit with a Gaussian. The value for  $\Delta f$  of the striation was found from the FWHM of the fitted peak was found to be  $\Delta f \sim 0.2$  MHz. The ratio of frequency to bandwidth for the striation was found to be  $\Delta f/f = 0.006$ , leading to an estimated source size of  $3.18''$ . Similar to [Kontar et al. \(2017\)](#), this is far smaller than the source size observed from the visibility fit.

In the following section we will discuss why the most probable cause for the discrepancy in source size is radio scattering, as well as a discussion on the comparison of this observation to recent developments in the theory and the effect scattering has had on actual source size and position.

## 4.4 Discussion

Adopting the theory described by [Takakura & Yousef \(1975\)](#) and used in [Kontar et al. \(2017\)](#), the predicted source sizes of a Type IIIb striation are much smaller than what

is observed. The most probable cause for this discrepancy is a combination of radio light scattering in the solar corona, propagation effects in the Earth’s ionosphere and limitations due to angular resolution. With this observation we accounted for and corrected ionospheric effects in the calibration step (Section 4.3 and [de Gasperin et al., 2019](#)) thereby removing the largest uncertainty in source size and position. By fitting the source size directly in visibility space we can directly see the power at which different angular scales were observed. The *uv* coverage of this observation allows angular scales of  $\sim 42''$  to be observed (Figure 4.2c) and although the predicted source size of  $\sim 3''$  is smaller than this, the amplitude of the observed visibilities does not increase until  $\sim 10'$  indicating that this is, in fact, the smallest source size observed in the visibilities.

It should be noted that there is better *uv* coverage along one axis compared to its orthogonal which may have an effect on the eccentricity of the elliptical Gaussian fit. However, owing to the qualitatively similar shape as predicted by [Kontar et al. \(2019\)](#) for a burst originating near the solar limb, we are confident that the eccentricity is representative of the real source. The orientation and elongation of the source are also consistent with observations of anisotropic scattering in the solar wind ([Anantharamaiah et al., 1994; Ingale et al., 2015](#)) where scattered sources are elongated perpendicular to the large scale (radial) magnetic field of the Sun.

Having accounted for all systematic effects that can affect the source size, we conclude that the large source sizes observed in this observation are due to the effect of scattering in the solar corona only. Previous tied-array observations have similar conclusions, however the tied-array technique interpolates data from a tessellation of beams across the Sun, and this introduces an ambiguity to the origin and size of sources. We assume the origin of the radio source to be somewhere above the active regions close to the East limb. An exploratory potential free source surface (PFSS) extrapolation suggests open field lines at an angle of  $\theta_s \sim 20^\circ$  from the plane of sky

#### 4. MEASURING SOURCE SIZES IN VISIBILITY SPACE

---

towards the observer. Similar to [Chrysaphi et al. \(2018\)](#) (Equations 5 and 6), we determine an out-of-plane heliocentric distance for the source. Using the observed in-plane heliocentric distance and an angle of  $\theta_s \sim 20^\circ$  from the plane of sky, we obtain an out-of-plane heliocentric distance of  $1.82 R_\odot$ . Comparing this to Figure 8 in [Kontar et al. \(2019\)](#), which shows the effect of the angle from the plane-of-sky  $\theta_s$  on source position and FWHM size in the major and minor axis, we would expect a ratio of the FWHM on the minor axis to the FWHM of the major axis to be of the order of 0.6. Our observations show a ratio of 0.54 suggesting  $\theta_s \sim 20^\circ$  is an appropriate approximation for the angle from the plane-of-sky.

The FWHM of the source at 34.76 MHz along the major and minor axis for this observation are  $18.8' \pm 0.1'$  and  $10.2' \pm 0.1'$  respectively. This gives the FWHM area of the source to be  $A_s = 150.6 \text{ arcmin}^2$ , which we note is smaller than that of [Kontar et al. \(2017\)](#) who measure  $A_s = 400 \text{ arcmin}^2$  at a similar frequency of 32.5 MHz. While this could be simply due to these being two separate observations, this may be more indicative of a discrepancy between source sizes measured in interferometric observations and tied-array observations. As mentioned in Section 4.3, the spatial resolution of LOFAR interferometric observations is superior to that of tied-array observations. This is mostly due to the additional stations that can be used for interferometric imaging and thus greater baseline lengths, but also due to the way tied-array images are made. Tied-array observations are carried out by pointing a number of beams in a honeycomb like pattern centred on the sun and interpolating data from each of the tessellated beams. The effect of this on observed source sizes and position is, as of yet, un-characterised. [Kontar et al. \(2017\)](#) attribute the large source size observed in their tied-array observation of a Type IIIb radio burst to the scattering of radio waves off of density inhomogeneities in the solar corona. It was later determined that a relative r.m.s fluctuation of electron density of  $\varepsilon = 0.8$  was necessary to explain the large source size observed [Kontar et al. \(2019\)](#). While it is evident that radio wave

scattering causes radio bursts to appear larger in observations than predicted, the reduced spatial resolution of tied-array imaging may result in an overestimate of  $\varepsilon$ .

The last decade has seen a renewed interest in low frequency observations of the radio sun with state of the art radio interferometers such as LOFAR and the MWA. Radio bursts emitted via the plasma emission process give a diagnostic of the local plasma density which may give insight into the turbulent nature of coronal plasma. It is theorised that the size of low frequency radio emission is limited by scattering caused by turbulence (Bastian, 1994), however it is only recently that the angular resolution necessary to challenge this theory has become available. In particular, a robust comparison of sources observed with tied-array and interferometric imaging is needed. Analytical approximations of radio scattering (e.g. Chrysaphi et al., 2018; Gordovskyy et al., 2019; Sharma & Oberoi, 2020) have seen some success in accounting for apparent source shift and brightness temperature due to scattering, however they cannot account for the anisotropic nature of scattering and may not be appropriate to describe large angle scattering near the source location. As such, a full numerical treatment of scattering (e.g. Bian et al., 2019; Kontar et al., 2019; Thejappa & MacDowall, 2008), in combination with interferometric imaging, is necessary to fully understand radio wave propagation in the turbulent coronal plasma. In order to definitively determine  $\varepsilon$ , more information on the power spectrum of density fluctuations and the scales on which radio scattering most effectively occurs is needed.

## 4.5 Conclusion

In summary, a Type IIIb radio burst was observed with LOFAR on 17 October 2015 at approximately 13:21:00 UTC. The bandwidth of an individual striation at 34.76 MHz suggests a FWHM source size of  $3.18''$ . Directly fitting visibilities to avoid effects of deconvolution algorithms reveals a FWHM source size in the major and minor axes

#### 4. MEASURING SOURCE SIZES IN VISIBILITY SPACE

---

of  $18.8' \pm 0.1'$  and  $10.2' \pm 0.1'$  respectively. The source is located at  $-1312'', -1064''$  from the solar centre. Having corrected for radio wave propagation in the ionosphere, we conclude that scattering from electron density fluctuations in the solar corona is the main cause of source broadening. We discuss how values for the r.m.s relative electron density fluctuations determined from numerical models and compared to tied-array observations may be an overestimate. In the future, a combination of remote observations from LOFAR and *in situ* measurements of plasma properties from PSP and Solar Orbiter ([Müller et al., 2020, 2013](#)) at a variety of heliocentric distances in the corona and solar wind will be needed to form a more complete picture of coronal turbulence.

# 5

## Scattering Observations vs Theory

In this chapter I utilise the direct visibility fitting method described in Chapter 4 and apply it to hundreds of type III radio bursts. I showcase the striking similarity between these observations and computational modelling.

## 5. SCATTERING OBSERVATIONS VS THEORY

# 6

## Future Work

This chapter is dedicated to the future of solar radio physics

### 6.1 TBB data

### 6.2 More Scattering



## References

- Amiri, M., Andersen, B. C., Bandura, K. M., et al. 2020, *Nature*, 582, 351 (Cited on page 44.)
- Amiri, M., Bandura, K., Berger, P., et al. 2018, *The Astrophysical Journal*, 863, 48 (Cited on page 42.)
- Anantharamaiah, K. R., Gothoskar, P., & Cornwell, T. J. 1994, *Journal of Astrophysics and Astronomy*, 15, 387 (Cited on page 69.)
- Andersen, B. C., Bandura, K., Bhardwaj, M., et al. 2019, *The Astrophysical Journal*, 885, L24 (Cited on page 44.)
- Appleton, E. & Hey, J. 1946, *The London, Edinburgh, and Dublin Philosophical Magazine and Journal of Science*, 37, 73 (Cited on page 19.)
- Aschwanden, M. J. 2004, *Physics of the Solar Corona* (Cited on page 3.)
- Bartosz, P. D., Flisek, P., Blaszkiewicz, L., & Shevchuk, M. 2020, in *Proceedings of the Polish Astronomical Society*, Vol. 10, 49–51 (Cited on page 45.)
- Bassa, C., Pleunis, Z., & Hessels, J. 2017, *Astronomy and Computing*, 18, 40 (Cited on page 36.)
- Bastian, T. S. 1994, *The Astrophysical Journal*, 426, 774 (Cited on pages 13 and 71.)
- Bhat, N. D. R., Cordes, J. M., & Chatterjee, S. 2003, *The Astrophysical Journal*, 584, 782 (Cited on page 42.)
- Bian, N. H., Emslie, A. G., & Kontar, E. P. 2019, *The Astrophysical Journal*, 873, 33 (Cited on page 71.)
- Bigg, E. K. 1964, *Nature*, 203 (Cited on page 47.)
- Bilous, A. V., Bondonneau, L., Kondratiev, V. I., et al. 2020, *Astronomy & Astrophysics*, 635, A75 (Cited on page 40.)
- Bilous, A. V., Hessels, J. W. T., Kondratiev, V. I., et al. 2014, *Astronomy & Astrophysics*, 572, A52 (Cited on page 40.)
- Bisoi, S. K., Janardhan, P., Ingale, M., et al. 2014, *The Astrophysical Journal*, 795, 69 (Cited on page 59.)
- Blaszkiewicz, L., Lewandowski, W., Smierciak, B., et al. 2020, in *Proceedings of the Polish Astronomical Society*, Vol. 10, 46–48 (Cited on page 40.)
- Boischot, A. & André. 1957, *Comptes Rendus de l'Académie des Sciences, Paris*, Vol. 244, p. 1326–1329, 244, 1326 (Cited on pages 20 and 45.)
- Bondonneau, L., Grießmeier, J. M., Theureau, G., et al. 2020, *Astronomy & Astrophysics* (submitted) [[arXiv]2009.02076] (Cited on page 29.)
- Bondonneau, L., Grießmeier, J.-M., Theureau, G., & Serylak, M. 2017, *Proceedings of the International Astronomical Union*, 13, 313 (Cited on pages 29 and 40.)
- Briggs, D. S. 1995, *American Astronomical Society, 187th AAS Meeting*, id.112.02; *Bulletin of the American Astronomical Society*, Vol. 27, p.1444, 187, 112.02 (Cited on page 63.)
- Broekema, P. C., Mol, J. J. D., Nijboer, R., et al. 2018, *Astronomy and Computing*, 23, 180 (Cited on page 26.)
- Burke, B. F. & Franklin, K. L. 1955, *Journal of Geophysical Research*, 60 (Cited on page 47.)
- Carley, E., Cecconi, B., Reid, H., et al. 2021, in *EGU General Assembly*, EGU21–13113 (Cited on page 45.)
- Carley, E. P., Baldovin, C., Benthem, P., et al. 2020, *Journal of Space Weather and Space Climate*, 10, 7 (Cited on page 53.)
- Carley, E. P., Hayes, L. A., Murray, S. A., et al. 2019, *Nature Communications*, 10, 2276 (Cited on page 47.)
- Carley, E. P., Reid, H., Vilmer, N., & Gallagher, P. T. 2015, *Astronomy & Astrophysics*, 581, A100 (Cited on page 47.)
- Chrysaphi, N., Kontar, E. P., Holman, G. D., & Temmer, M. 2018, *The Astrophysical Journal*, 868, 79 (Cited on pages 70 and 71.)
- Clarke, B. P., Morosan, D. E., Gallagher, P. T., et al. 2019 [[arXiv]1901.07424] (Cited on page 10.)
- Cliver, E. W. & Ling, A. G. 2009, *The Astrophysical Journal*, 690, 598 (Cited on page 7.)
- Cornwell, T. J. 2008, *IEEE Journal on Selected Topics in Signal Processing*, 2, 793 (Cited on page 63.)
- de Gasperin, F., Dijkema, T. J., Drabent, A., et al. 2019, *Astronomy & Astrophysics*, 622, A5 (Cited on pages 61, 63 and 69.)
- de La Noe, J. 1975, *Astronomy and Astrophysics*, 43, 201 (Cited on page 58.)
- de La Noe, J. & Boischot, A. 1972, *Astronomy and Astrophysics*, 20, 55 (Cited on page 58.)

- Dewdney, P. E., Hall, P. J., Schilizzi, R. T., & Lazio, T. J. L. 2009, Proceedings of the IEEE, 97, 1482 (Cited on page 60.)
- Donner, J. Y., Verbiest, J. P. W., Tiburzi, C., et al. 2019, *Astronomy & Astrophysics*, 624, A22 (Cited on pages 29 and 40.)
- Driessen, L. N., Janssen, G. H., Bassa, C. G., Stappers, B. W., & Stinebring, D. R. 2019, *Monthly Notices of the Royal Astronomical Society*, 483, 1224 (Cited on page 42.)
- Edler, H. W., de Gasperin, F., & Rafferty, D. 2021, *Astronomy & Astrophysics*, 652, A37 (Cited on page 54.)
- Ellis, G. 1969, *Australian Journal of Physics*, 22, 177 (Cited on pages 9, 47 and 58.)
- Ellis, G. & McCulloch, P. 1967, *Australian Journal of Physics*, 20, 583 (Cited on pages 47 and 58.)
- Enriquez, J. E., Siemion, A., Foster, G., et al. 2017, *The Astrophysical Journal*, 849, 104 (Cited on page 51.)
- Fokker, A. D. 1965, *Bulletin of the Astronomical Institutes of the Netherlands*, 18, 111 (Cited on pages 57 and 58.)
- Foukal, P. V. 2004, *Solar Astrophysics*, 480 (Cited on page 1.)
- Fox, N. J., Velli, M. C., Bale, S. D., et al. 2016, *Space Science Reviews*, 204, 7 (Cited on page 59.)
- Gajjar, V., Siemion, A., Croft, S., et al. 2019, *Bulletin of the AAS*, 51 [[arXiv]1907.05519] (Cited on page 51.)
- Ginzburg, V. L. & Zhelezniakov, V. V. 1958, *Astronomicheskii Zhurnal*, 35, 694 (Cited on pages 10, 20, 23 and 45.)
- Gopalswamy, N. & Thompson, B. 2000, *Journal of Atmospheric and Solar-Terrestrial Physics*, 62, 1457 (Cited on page 5.)
- Gordovskyy, M., Kontar, E., Browning, P., & Kuznetsov, A. 2019, *The Astrophysical Journal*, 873, 48 (Cited on pages 58 and 71.)
- Hankins, T. H. & Rajkowski, J. M. 1987, *Review of Scientific Instruments*, 58, 674 (Cited on page 36.)
- Hermsen, W., Kuiper, L., Basu, R., et al. 2018, *Monthly Notices of the Royal Astronomical Society*, 480, 3655 (Cited on pages 29 and 40.)
- Hess, S., Mottez, F., & Zarka, P. 2009, *Geophysical Research Letters*, 36, L14101 (Cited on page 50.)
- Hess, S., Zarka, P., & Mottez, F. 2007, *Planetary and Space Science*, 55, 89 (Cited on page 50.)
- Högberg, J. A. 1974, *Astronomy & Astrophysics Supplemental*, 15, 417 (Cited on page 63.)
- Hotan, A. W., van Straten, W., & Manchester, R. N. 2004, *Publications of the Astronomical Society of Australia*, 21, 302 (Cited on page 36.)
- Hurford, G. J., Schmahl, E. J., Schwartz, R. A., et al. 2002, *Solar Physics*, 210, 61 (Cited on page 64.)
- Ingale, M., Subramanian, P., & Cairns, I. 2015, *Monthly Notices of the Royal Astronomical Society*, 447, 3486 (Cited on page 69.)
- Isaacson, H., Siemion, A. P., Marcy, G. W., et al. 2017, *Publications of the Astronomical Society of the Pacific*, 129, 054501 (Cited on page 51.)
- Jameson, A. & van Straten, W. 2008, PSRDADA: Data Acquisition and Distributed Analysis Software <https://researchdata.edu.au/psrdada-acquisition-distributed-analysis-software/185603> (Cited on page 54.)
- Johnston, S., Taylor, R., Bailes, M., et al. 2008, *Experimental Astronomy*, 22, 151 (Cited on page 26.)
- Jonas, J. 2018, in *Proceedings of MeerKAT Science: On the Pathway to the SKA — PoS(MeerKAT2016)* (Trieste, Italy: Sissa Medialab), 001 (Cited on page 26.)
- Karako-Argaman, C., Kaspi, V. M., Lynch, R. S., et al. 2015, *The Astrophysical Journal*, 809, 67 (Cited on page 42.)
- Karastergiou, A., Chennamangalam, J., Armour, W., et al. 2015 [[arXiv]1506.03370] (Cited on pages 29 and 44.)
- Karuppusamy, R., Stappers, B. W., & Lee, K. J. 2012, *Astronomy and Astrophysics*, 538, A7 (Cited on page 41.)
- Keane, E. F. 2018, *Nature Astronomy*, 2, 865 (Cited on page 38.)
- Keane, E. F., Kramer, M., Lyne, A. G., et al. 2011, *Monthly Notices of the Royal Astronomical Society*, 415, 3065 (Cited on page 42.)
- Kolotkov, D. Y., Nakariakov, V. M., & Kontar, E. P. 2018, *The Astrophysical Journal*, 861, 33 (Cited on page 45.)
- Kontar, E. P., Chen, X., Chrysaphi, N., et al. 2019, *The Astrophysical Journal*, 884, 122 (Cited on pages 57, 58, 59, 69, 70 and 71.)
- Kontar, E. P., Hannah, I. G., Jeffrey, N. L. S., & Battaglia, M. 2010, *The Astrophysical Journal*, 717, 250 (Cited on page 64.)
- Kontar, E. P., Yu, S., Kuznetsov, A. A., et al. 2017, *Nature Communications*, 8, 1515 (Cited on pages 7, 13, 58, 59, 60, 61, 68 and 70.)
- Krupar, V., Maksimovic, M., Kontar, E. P., et al. 2018, *The Astrophysical Journal*, 857, 82 (Cited on pages 58 and 59.)
- Krupar, V., Szabo, A., Maksimovic, M., et al. 2020 [[arXiv]2001.03476] (Cited on page 59.)
- Lebofsky, M., Croft, S., Siemion, A. P., et al. 2019, *Publications of the Astronomical Society of the Pacific*, 131, 124505 (Cited on page 37.)

- Lemen, J. R., Title, A. M., Akin, D. J., et al. 2012, Solar Physics, 275, 17 (Cited on page 65.)
- Lonsdale, C. J., Cappallo, R. J., Morales, M. F., et al. 2009, Proceedings of the IEEE, 97, 1497 (Cited on pages 26 and 60.)
- Lorimer, D. 2011, SIGPROC: Pulsar Signal Processing Programs <http://ascl.net/1107.016> (Cited on page 36.)
- Lorimer, D. R., Bailes, M., McLaughlin, M. A., Narkevic, D. J., & Crawford, F. 2007, Science, 318, 777 (Cited on pages 37 and 44.)
- Louarn, P., Allegrini, F., McComas, D. J., et al. 2017, Geophysical Research Letters, 44, 4439 (Cited on page 47.)
- Lubberhuizen, W. & Kooistra, E. 2009, RSP - CEP Beamlet Data Interface. Technical Report LOFAR-ASTRON-SDD-009, Tech. rep. (Cited on page 30.)
- Lyne, A. G., Jordan, C. A., Graham-Smith, F., et al. 2015, Monthly Notices of the Royal Astronomical Society, 446, 857 (Cited on page 41.)
- Maguire, C. A., Carley, E. P., McCauley, J., & Gallagher, P. T. 2020, Astronomy & Astrophysics, 633, A56 (Cited on pages 29, 39 and 45.)
- Malville, J. M. & M., J. 1962, The Astrophysical Journal, 135, 834 (Cited on page 20.)
- Manchester, R. N. 2017, Journal of Physics: Conference Series, 932, 012002 (Cited on page 38.)
- Mann, G. 1995, in Lecture Notes in Physics, Berlin Springer Verlag, Vol. 444, Coronal Magnetic Energy Releases, ed. A. Benz & A. Krüger, 183 (Cited on page 8.)
- Marques, M. S., Zarka, P., Echer, E., et al. 2017, Astronomy and Astrophysics, 604 (Cited on page 50.)
- McConnell, D. 1980, Publications of the Astronomical Society of Australia, 4, 64 (Cited on pages 7, 10 and 13.)
- McKay-Bukowski, D., Vierinen, J., Virtanen, I. I., et al. 2015, KAIRA: The Kilpisjärvi atmospheric imaging receiver array - System overview and first results (Cited on page 28.)
- McKee, J. W., Lyne, A. G., Stappers, B. W., Bassa, C. G., & Jordan, C. A. 2018, Monthly Notices of the Royal Astronomical Society, 479, 4216 (Cited on page 42.)
- McKenna, D. 2020 (Cited on page 35.)
- McLaughlin, M. A., Lyne, A. G., Lorimer, D. R., et al. 2006, Nature, 439, 817 (Cited on page 37.)
- McLean, D. J. & Labrum, N. R. 1985, Cambridge and New York, Cambridge University Press, 1985, 527 p. For individual items see A87-13852 to A87-13867. (Cited on pages 20 and 58.)
- McMullin, J. P., Diamond, P. J., McPherson, A. M., et al. 2020, in SPIE, Vol. 11445 (SPIE-Intl Soc Optical Eng), 243 (Cited on page 26.)
- Melnik, V. N., Konovalenko, A. A., Rucker, H. O., et al. 2010a, Solar Physics, 264, 103 (Cited on pages 10 and 47.)
- Melnik, V. N., Rucker, H. O., Konovalenko, A. A., et al. 2010b, in AIP Conference Proceedings, Vol. 1206, 445–449 (Cited on page 58.)
- Melrose, D. B. 1982, Solar Radio Storms, CESRA Workshop #4, 182 (Cited on page 7.)
- Melrose, D. B. 1987, Solar Physics, 111, 89 (Cited on pages 21 and 45.)
- Mereghetti, S., Kuiper, L., Tiengo, A., et al. 2016, The Astrophysical Journal, 831, 21 (Cited on pages 29 and 40.)
- Meyers, B. W., Tremblay, S. E., Bhat, N. D. R., et al. 2017, The Astrophysical Journal, 851, 20 (Cited on pages 41 and 42.)
- Michilli, D., Bassa, C., Cooper, S., et al. 2020, Monthly Notices of the Royal Astronomical Society, 491, 725 (Cited on page 42.)
- Michilli, D., Hessels, J. W. T., Donner, J. Y., et al. 2018, Monthly Notices of the Royal Astronomical Society, 476, 2704 (Cited on page 29.)
- Mickaliger, M. B., Stappers, B. W., Bassa, C. G., & Fletcher, A. G. 2017, Proceedings of the International Astronomical Union, 13, 380 (Cited on page 42.)
- Mondal, S., Oberoi, D., & Mohan, A. 2020, The Astrophysical Journal, 895, L39 (Cited on page 45.)
- Morosan, D. E., Carley, E. P., Hayes, L. A., et al. 2019a, Nature Astronomy, 3, 452 (Cited on page 61.)
- Morosan, D. E., Gallagher, P. T., Zucca, P., et al. 2014, Astronomy & Astrophysics, 568, A67 (Cited on page 61.)
- Morosan, D. E., Gallagher, P. T., Zucca, P., et al. 2015, Astronomy & Astrophysics, 580, A65 (Cited on page 10.)
- Morosan, D. E., Kilpuua, E. K. J., Carley, E. P., & Monstein, C. 2019b [[arXiv:1902.01140](https://arxiv.org/abs/1902.01140)] (Cited on pages 39 and 45.)
- Müller, D., Cyr, O. C. S., Zouganelis, I., et al. 2020, Astronomy & Astrophysics, 642, A1 (Cited on page 72.)
- Müller, D., Marsden, R. G., St. Cyr, O. C., & Gilbert, H. R. 2013, Solar Physics, 285, 25 (Cited on page 72.)
- Murphy, P. C., Carley, E. P., Ryan, A. M., Zucca, P., & Gallagher, P. T. 2021, Astronomy and Astrophysics, 645, A11 (Cited on page 45.)
- Nelson, G. & Melrose, D. 1985, in Solar Radiophysics: Studies of Emission from the Sun at Metre Wavelengths, ed. D. McLean & N. Labrum, 333–359 (Cited on pages 7, 8 and 9.)

- Noutsos, A., Sobey, C., Kondratiev, V. I., et al. 2015, *Astronomy & Astrophysics*, 576, A62 (Cited on page 40.)
- Offringa, A. R., McKinley, B., Hurley-Walker, N., et al. 2014, *Monthly Notices of the Royal Astronomical Society*, 444, 606 (Cited on page 63.)
- Offringa, A. R. & Smirnov, O. 2017 [[arXiv]1706.06786] (Cited on page 63.)
- Pastor-Marazuela, I., Connor, L., van Leeuwen, J., et al. 2020, arXiv [[arXiv]2012.08348] (Cited on page 44.)
- Pick, M. & Vilmer, N. 2008, *Astronomy and Astrophysics Review*, 16, 1 (Cited on page 45.)
- Pleunis, Z., Michilli, D., Bassa, C. G., et al. 2021, *The Astrophysical Journal Letters*, 911, L3 (Cited on page 45.)
- Porayko, N. K., Noutsos, A., Tiburzi, C., et al. 2019, *Monthly Notices of the Royal Astronomical Society*, 483, 4100 (Cited on page 29.)
- Postel, J. 1980, Internet Protocol, RFC 768, USC/Information Sciences Institute (Cited on page 30.)
- Rajwade, K., Seymour, A., Lorimer, D. R., et al. 2016, *Monthly Notices of the Royal Astronomical Society*, 462, 2518 (Cited on page 29.)
- Ransom, S. M. 2001, PhD thesis, Harvard University (Cited on page 36.)
- Reid, H. A. & Kontar, E. P. 2017, *Astronomy and Astrophysics*, 606 [[arXiv]1706.07410] (Cited on pages 12 and 61.)
- Reid, H. A. S. & Kontar, E. P. 2010, *The Astrophysical Journal*, 721, 864 (Cited on page 59.)
- Reid, H. A. S. & Kontar, E. P. 2018, *Astronomy & Astrophysics*, 614, A69 (Cited on page 47.)
- Reid, H. A. S. & Kontar, E. P. 2021, *Nature Astronomy*, 5, 796 (Cited on page 45.)
- Reid, H. A. S. & Ratcliffe, H. 2014, *Research in Astronomy and Astrophysics*, 14, 773 (Cited on pages 10, 21, 22, 47, 58 and 64.)
- Reiner, M., Kaiser, M., Fainberg, J., Bougeret, J.-L., & Stone, R. 1997, in *ESA Special Publication*, Vol. 415, Correlated Phenomena at the Sun, in the Heliosphere and in Geospace, ed. A. Wilson, 183 (Cited on page 9.)
- Riddle, A. C. 1974, *Solar Physics*, 35, 153 (Cited on pages 13, 57 and 58.)
- Sanidas, S., Cooper, S., Bassa, C. G., et al. 2019, *Astronomy & Astrophysics*, 626, A104 (Cited on page 42.)
- Sasikumar Raja, K., Ingale, M., Ramesh, R., et al. 2016 [[arXiv]1611.04282] (Cited on page 59.)
- Scaife, A. M. M. 2020, *Philosophical Transactions of the Royal Society A: Mathematical, Physical and Engineering Sciences*, 378 (Cited on page 26.)
- Schoonderbeek, G. W., Szomoru, A., Gunst, A. W., Hiemstra, L., & Hargreaves, J. 2019, *Journal of Astronomical Instrumentation*, 08, 1950003 (Cited on page 53.)
- Scully, J., Flynn, R., Carley, E., Gallagher, P., & Daly, M. 2021, in *2021 32nd Irish Signals and Systems Conference (ISSC)* (IEEE), 1–6 (Cited on page 40.)
- Serylak, M., Karastergiou, A., Williams, C., Armour, W., & Giles, M. 2012in , 492–494 (Cited on page 29.)
- Sharma, R. & Oberoi, D. 2020 [[arXiv]2009.10604] (Cited on page 71.)
- Sharykin, I. N., Kontar, E. P., & Kuznetsov, A. A. 2018a, *Solar Physics*, 293, 115 (Cited on page 45.)
- Sharykin, I. N., Kontar, E. P., & Kuznetsov, A. A. 2018b, *Solar Physics*, 293, 115 (Cited on page 58.)
- Smerd, S., Sheridan, K., & Stewart, R. 1974, in *IAU Symposium*, Vol. 57, Coronal Disturbances, ed. G. Newkirk, 389 (Cited on page 8.)
- Stappers, B. W., Hessels, J. W. T., Alexov, A., et al. 2011, *Astronomy & Astrophysics*, 530, A80 (Cited on page 40.)
- Steinberg, J. L., Aubier-Giraud, M., Leblanc, Y., & Boischot, A. 1971, *Astronomy and Astrophysics*, 10, 362 (Cited on pages 57 and 58.)
- Stewart, R. T. 1972, *Publications of the Astronomical Society of Australia*, 2, 100 (Cited on pages 57 and 58.)
- Takakura, T. & Yousef, S. 1975, *Solar Physics*, 40, 421 (Cited on pages 59 and 68.)
- Tan, C. M., Bassa, C. G., Cooper, S., et al. 2020, *Monthly Notices of the Royal Astronomical Society*, 492, 5878 (Cited on page 42.)
- Tarter, J. 2001, *Annual Review of Astronomy and Astrophysics*, 39, 511 (Cited on page 37.)
- ter Veen, S., Enriquez, J. E., Falcke, H., et al. 2019, *Astronomy & Astrophysics*, 621, A57 (Cited on page 44.)
- Thejappa, G. & MacDowall, R. J. 2008, *The Astrophysical Journal*, 676, 1338 (Cited on pages 57, 58 and 71.)
- Thejappa, G., MacDowall, R. J., & Kaiser, M. L. 2007, *The Astrophysical Journal*, 671, 894 (Cited on pages 57 and 58.)
- Thornton, D., Stappers, B., Bailes, M., et al. 2013, *Science*, 341, 53 (Cited on page 37.)
- Tiburzi, C., Verbiest, J. P. W., Shaifullah, G. M., et al. 2019, *Monthly Notices of the Royal Astronomical Society*, 487, 394 (Cited on page 29.)
- Treumann, R. A. 2006, *The Astronomy and Astrophysics Review*, 13, 229 (Cited on page 47.)

- Turner, J. D., Grießmeier, J.-M., Zarka, P., & Vasylyeva, I. 2019, *Astronomy & Astrophysics*, 624, A40 (Cited on page 49.)
- Turner, J. D., Zarka, P., Grießmeier, J.-M., et al. 2021, *Astronomy & Astrophysics*, 645, A59 (Cited on page 49.)
- van Diepen, G., Dijkema, T. J., & Offringa, A. 2018, *ascl*, ascl:1804.003 (Cited on page 63.)
- van Haarlem, M. P., Wise, M. W., Gunst, A. W., et al. 2013, *Astronomy & Astrophysics*, Volume 556, id.A2, 53 pp., 556 [[arXiv]1305.3550] (Cited on pages 20, 26, 27, 28, 39 and 50.)
- Van Leeuwen, J., Mikhailov, K., Keane, E., et al. 2020, *Astronomy and Astrophysics*, 634, A3 (Cited on page 41.)
- van Straten, W. & Bailes, M. 2011, *Publications of the Astronomical Society of Australia*, 28, 1 (Cited on page 36.)
- Vedenov, A. A. 1963, *Journal of Nuclear Energy. Part C, Plasma Physics, Accelerators, Thermonuclear Research*, 5, 169 (Cited on page 21.)
- Virtanen, I. I. 2018, *ASTRON document LOFAR-ASTRON-MAN-064*, 51 (Cited on page 30.)
- Voronkov, M. 2020, *EPJ Web of Conferences*, 245, 01038 (Cited on page 26.)
- Vršnak, B., Magdalenić, J., Aurass, H., & Mann, G. 2002, *Astronomy & Astrophysics*, 396, 673 (Cited on page 8.)
- Wild, J. P. 1950, *Australian Journal of Chemistry*, 3, 399 (Cited on page 6.)
- Wild, J. P. & McCready, L. L. 1950, *Australian Journal of Scientific Research A*, vol. 3, p.387, 3, 387 (Cited on pages 20 and 45.)
- Wild, J. P., Sheridan, K. V., & Trent, G. H. 1959, *URSI Symp. 1: Paris Symposium on Radio Astronomy*, 9, 176 (Cited on pages 20 and 45.)
- Worden, S. P., Drew, J., Siemion, A., et al. 2017, *Acta Astronautica*, 139, 98 (Cited on page 51.)
- Wu, C. 1985, *Space Science Reviews*, 41, 215 (Cited on page 49.)
- Wu, C. S. & Lee, L. C. 1979, *The Astrophysical Journal*, 230, 621 (Cited on page 49.)
- Wucknitz, O. 2019, in *Proceedings of 14th European VLBI Network Symposium & Users Meeting — PoS(EVN2018)*, Vol. 344 (Trieste, Italy: Sissa Medialab), 017 (Cited on page 39.)
- Zarka, P. 1998, *Journal of Geophysical Research: Planets*, 103, 20159 (Cited on page 49.)
- Zhang, P., Zucca, P., Sridhar, S. S., et al. 2020 [[arXiv]2005.09419] (Cited on pages 45 and 47.)
- Zucca, P., Carley, E. P., McCauley, J., et al. 2012, *Solar Physics*, 280, 591 (Cited on pages vii, 11 and 12.)
- Zucca, P., Morosan, D. E., Rouillard, A. P., et al. 2018, *Astronomy & Astrophysics*, 615, A89 (Cited on page 61.)